Hindawi
International Journal of Aerospace Engineering
Volume 2022, Article ID 9443050, 25 pages
https://doi.org/10.1155/2022/9443050

Research Article

Boost-Phase Trajectory Planning with the Nonregular Reachable Area Constraints

Yin Diao, Rongjun Mu, Yingzi Guan, and Naigang Cui

School of Astronautics, Harbin Institute of Technology, Harbin 150001, China

Correspondence should be addressed to Yingzi Guan; guanyz@hit.edu.cn

Received 11 November 2021; Revised 29 March 2022; Accepted 2 June 2022; Published 26 June 2022

Academic Editor: Jacopo Serafini

During emergency return or mission change, the boost-glide vehicle needs to meet the nonregular reachable area constraints (NRACs). Therefore, this paper introduced NRACs into boost-phase trajectory planning to extend the maneuvering range and enhance the mission adaptability of boost-glide vehicle. Firstly, the library of the reachable area boundaries was constructed with the fast computation method under the deviations of boost terminal states, and the polynomials were used to fit the boundary parameters. Secondly, the nonlinear mapping relationship between the reachable area boundary parameters and the deviations of boost terminal states was obtained by the deep neural networks (DNNs). Then, the new boundary parameters were obtained by the constraint transformation rules under NRACs and the separation window constraints and transformed into the constraints of the boost-phase terminal states by DNNs. Finally, the hp-adaptive pseudospectral method (hpPM) was adopted to complete the trajectory planning considering the path and terminal constraints. The simulation results showed that the proposed trajectory planning method considering NRACs had high trajectory planning accuracy and good deviation adaptability and exhibited excellent performance in the adjustment of reachable area. This study provides theoretical support for integrate mission decisions and trajectory planning of boost-glide vehicles.

1. Introduction

Proposed by X. S. Qian in 1948, boost-glide vehicles, characterized with high lift-to-drag ratio, high altitude and velocity, and large flight envelope, are capable of long-range maneuvering, defense penetration, and target changing [1]. Diversified launch modes and multistage boosters have greatly expanded the glider's application scope. In particular, the air-based launch mode allows the glider to quickly obtain the initial states in a specified direction, which brings great convenience for mission expansion. To reach the designated mission area precisely, suitable initial conditions of the glider are required for the boost-phase trajectory planning. Compared with the gliding phase, the boost phase is characterized by shorter flight time and weaker mobility, and it can significantly affect the reachable area by changing the initial conditions of the glider. Therefore, boost-phase trajectory planning has become one of the critical technologies affecting mission reachability.

Under the preset separation conditions, boost-glide vehicles only depend on the gliding phase trajectory planning to meet the landing point constraints. In the case of emergency return of lift-body spacecraft with a booster during the ascending phase or in the case of the terminal mission change of the boost-glide vehicle during the boost stage, the spacecraft or the vehicle needs to meet the temporary constraints of terminal reachable area, and the adjustment ability of the gliding phase may not be enough to meet the constraints. Therefore, the authors consider using the remaining fuel in the booster to replan the boost-phase trajectory, make the glider reach more appropriate separation conditions, and make full use of the maneuverability of different flight phases to meet the terminal constraints. At the same time, the boost-phase trajectory is affected by the initial state of the vehicle, the combined action of aerodynamic force and engine thrust, and the environmental disturbances and needs to satisfy various constraints such as process state quantity, control

angle, angular rate, and the quantity of terminal state quantity. Therefore, boost-phase trajectory planning is a complex practical problem to be addressed.

With the rapid development of trajectory optimization theory [2–4], trajectory planning methods are mainly divided into methods based on optimal control principle, optimization theory, and artificial intelligence technology. Among them, the methods based on optimization theory have advantages in flexibility, but the online computing performance under complex constraints needs to be improved; the methods based on artificial intelligence technology have advantages in efficiency and adaptability [5]. The multiconstraint trajectory planning problem can be better solved with the rapid development of optimization theory and artificial intelligence technology [6]. In literature [7], a full-phase optimization model of the boost-glide vehicle was established, and the furthest range trajectory planning problem was solved via segment optimization. In literature [8–10], the gliding-phase trajectory planning problem satisfying the range and path constraints was investigated. In literature [11], the orthogonal test method was used to determine the optimal initial glide conditions and effective results were obtained. However, the connection between the reachable area and the boost terminal states was not established. In literature [12], the solution of the reachable area was transformed into a series of longest ranges to the virtual target points, and the optimal control theory and quasi-equilibrium glide condition were adopted to turn the longest ranges into univariate iterative problems, so that high computational accuracy and convergence speed were obtained. However, the actual coverage requirements were not considered in the boost-phase trajectory planning.

DNNs/heuristic-based trajectory optimization algorithms have been widely studied. In reference [13, 14], a two-step strategy based on the trajectory optimization method and DNN attitude controller was proposed, which could better solve the problems in real-time attitude and trajectory planning and control for hypersonic vehicles. The desensitized/multiobjective trajectory optimization method generated the optimal reentry trajectory. In contrast, DNNs were used to obtain the optimal control attitude command matching the states, which could not realize the feedback from the reachable area constraints to the boost terminal states. Moreover, the thrust was not considered in the optimization model, so it could not be applied to the powered boost-phase trajectory optimization. In reference [15], a stochastic trajectory optimization framework was proposed to solve chance constraints, which could be used for the reentry trajectory planning of hypersonic vehicles under noise-perturbed dynamics and probabilistic constraints. In reference [16], a hybrid optimization algorithm composed of an initial value generator and an internal solver was proposed, which showed improved the convergence and stability. However, the algorithm proposed could not quickly calculate and adjust the reachable area.

Although heuristic algorithms such as the multiobjective genetic algorithm [17] and gray wolf algorithm [18] have been widely studied and developed, the pseudospectral method is still one of the mainstream algorithms applied in the field of ascending trajectory planning [19]. On the basis of the equivalence between the Karush-Kuhn-Tucker (KKT) conditions of the parametric nonlinear program problem (NLP) and the discrete Hamiltonian boundary value problem (HBVP) [20], the Gaussian pseudospectral method with higher accuracy and convergence speed has been widely used in the boost-phase trajectory planning [21, 22]. With ever-increasing solution scale of trajectory planning problem under complex constraints in recent years, the hp-adaptive discrete grid updating method has been integrated into the Gaussian/Radau pseudospectral method for trajectory planning [23].

To extend the maneuvering range of the boost-glide vehicle and meet NRACs, parametric descriptions of the reachable area, reachable area constraint transformation, and the boost-phase trajectory planning were studied in this paper. The main contributions of the work in this paper are drawn from the following three aspects.

(1) The NRACs were introduced into the boost-phase trajectory planning via constraint transformation to extend the maneuvering range and enhance mission adaptability

(2) A parametric method was designed to describe the reachable area boundary of the boost-glider vehicle, and DNNs were adopted to obtain the mapping relationship between the reachable area boundary and the booster's separation point states

(3) The energy equivalence principles were proposed to deal with the separation window constraints, and the hp-adaptive pseudospectral method was adopted to plan the trajectory under path and terminal constraints

The remainder of this paper is organized as follows. Firstly, the problem formulation and methodological framework are established in Section 2. Secondly, the reachable area boundary library is established by the reachable area fast calculation method under initial deviations of states and environmental perturbations. And the boundaries of the reachable area are parameterized by the polynomial in Section 3. Next, constraints transformation rules, relational mapping of deep neural networks, and energy equivalence principles are proposed to transform the nonregular reachable area constraints into the terminal state constraints of the boost phase in Section 4. Then, the hpPM is adopted to plan the boost-phase trajectory under the path and terminal constraints in Section 5. Finally, the simulation analyses of the proposed method are carried out under the nonregular reachable area constraints in Section 6.

2. Problem Formulation and Methodological Framework

2.1. Problem Formulation. The boost-glide vehicle has two flight phases: the boost phase and gliding phase. The

mathematical motion model of the boost phase can be established in the launch coordinate system as follows [24].

$$\begin{cases} m\dot{\mathbf{v}} = G_B \begin{bmatrix} P \\ 0 \\ 0 \end{bmatrix} + G_V \begin{bmatrix} -C_x q S_M \\ C_y q S_M \\ C_z q S_M \end{bmatrix} + m\dfrac{g_r'}{r} \begin{bmatrix} x + R_{0x} \\ y + R_{0y} \\ z + R_{0z} \end{bmatrix} + m\dfrac{g_{\omega_e}}{\omega_e} \begin{bmatrix} \omega_{ex} \\ \omega_{ey} \\ \omega_{ez} \end{bmatrix} - \\ m \begin{bmatrix} \omega_{ex}^2 - \omega_e^2 & \omega_{ex}\omega_{ey} & \omega_{ex}\omega_{ez} \\ \omega_{ex}\omega_{ey} & \omega_{ey}^2 - \omega_e^2 & \omega_{ez}\omega_{ey} \\ \omega_{ex}\omega_{ez} & \omega_{ez}\omega_{ey} & \omega_{ez}^2 - \omega_e^2 \end{bmatrix} \begin{bmatrix} x + R_{0x} \\ y + R_{0y} \\ z + R_{0z} \end{bmatrix} - m \begin{bmatrix} 0 & -2\omega_{ez} & 2\omega_{ey} \\ 2\omega_{ez} & 0 & -2\omega_{ex} \\ -2\omega_{ey} & 2\omega_{ex} & 0 \end{bmatrix} \begin{bmatrix} \dot{x} \\ \dot{y} \\ \dot{z} \end{bmatrix} \\ [\dot{x}\ \dot{y}\ \dot{z}]' = \mathbf{v}\dot{m} = -\dfrac{P}{I_{\text{sp}} g_0}, \end{cases} \tag{1}$$

where $\mathbf{v}$ denotes the velocity vector; x, y, and z denote the three components of position, respectively; G_B and G_V denote the transformation matrix from the body-fixed coordinate system and velocity coordinate system to the launch coordinate system, respectively; P denotes the engine's thrust; C_x, C_y, and C_z denote the drag, lift, and lateral force coefficients, respectively; q and S_M denote the dynamic pressure and pneumatic reference area, respectively; r and ω_e (which can be decomposed into ω_{ex}, ω_{ey}, and ω_{ez}) denote the geocentric vector diameter and earth rotation rate, respectively; g_r' and g_{ω_e} denote the gravitational components along the direction of the geocentric vector and the direction of the earth's rotation, respectively; g_0 is the gravitational acceleration at sea level; I_{sp} is specific impulse; $\dot{m}$ is engine consumption per second.

The dynamics model of the gliding phase is given as follows [12].

$$\begin{cases} \dot{r} = V \sin\gamma, \\ \dot{\theta} = \dfrac{V\cos\gamma\sin\psi}{r\cos\varphi}, \\ \dot{\varphi} = \dfrac{V\cos\gamma\cos\psi}{r}, \\ \dot{V} = -\dfrac{D}{m} + g_r\sin\gamma + g_\omega(\sin\gamma\sin\varphi + \cos\varphi\cos\psi\cos\gamma) + \\ r\omega_E^2\cos\varphi(\cos\varphi\sin\gamma - \cos\gamma\sin\varphi\cos\psi), \\ \dot{\gamma} = \dfrac{L\cos\sigma}{mV} + \dfrac{V}{r}\cos\gamma + \dfrac{g_r}{V}\cos\gamma + \dfrac{g_\omega}{V}(\sin\varphi\cos\gamma - \cos\varphi\cos\psi\sin\gamma) + \\ 2\omega_E\sin\psi\cos\varphi + \dfrac{\omega_E^2 r\cos\varphi}{V}(\cos\varphi\cos\gamma + \sin\varphi\cos\psi\sin\gamma), \\ \dot{\psi} = \dfrac{L\sin\sigma}{mV\cos\gamma} + \dfrac{V}{r}\cos\gamma\sin\psi\tan\varphi - \dfrac{g_\omega}{V\cos\gamma}\cos\varphi\sin\psi - \\ 2\omega_E(\tan\gamma\cos\psi\cos\varphi - \sin\varphi) + \dfrac{\omega_E^2 r}{V\cos\gamma}\sin\psi\sin\varphi\cos\varphi, \end{cases} \tag{2}$$

where $r = R_e + h$; R_e denotes the radius of the earth, and h is the height; L and D denote the aerodynamic lift and drag, respectively; θ and φ denote the latitude and longitude, respectively; V is the velocity; γ and ψ denote the flight path angle and heading angle, respectively.

The state equations of the boost terminal point need to be introduced to ensure the continuity of the motion equation.

$$\begin{cases} V = \sqrt{v_x^2 + v_y^2 + v_z^2}, \\ r = \sqrt{(x + R_{0x})^2 + (y + R_{0y})^2 + (z + R_{0z})^2}, \\ \varphi = \arcsin\left(\dfrac{\mathbf{r}\cdot\boldsymbol{\omega}_e}{r\omega_e}\right), \\ \theta = \arctan\left(\dfrac{r_{dy}}{r_{dx}}\right), \\ \gamma = \arctan\left(\dfrac{v_y}{v_x}\right), \\ \psi = \arctan\left(\dfrac{v_{\text{ENU}x}}{v_{\text{ENU}y}}\right), \end{cases} \tag{3}$$

where r_{dx} and r_{dy} denote the geocentric distance components in the X and Y directions in the geocentric coordinate system, respectively; v_{ENUx} and v_{ENUy} denote the velocity vector components in the X and Y directions in the local Cartesian coordinate coordinate system (ENU), respectively.

G_D denotes the coordinate conversion matrix from the launch coordinate system to the geocentric coordinate system, G_E denotes the coordinate conversion matrix from the geocentric coordinate system to ENU. G_D, G_E, G_B, and G_V can be represented as follows [24].

$$\begin{cases} G_D = L_y(-(90^\circ + A_0))L_x(\varphi_0)L_z(-(90^\circ - \theta_0)), \\ G_E = L_z(180^\circ)L_y(90^\circ)L_y(-\varphi)L_z(\theta), \\ G_B = L_x(\gamma_a)L_y(\psi_a)L_z(\varphi_a),\ G_V = L_x(\nu)L_y(\sigma_v)L_z(\theta_v), \end{cases} \tag{4}$$

where $L_i(\Delta), i = x, y, z$ is the direction cosine matrix of Δ rotation about i axis; φ_a, ψ_a, and γ_a denote the pitch angle, yaw angle, and roll angle, respectively; θ_v, σ_v, and ν denote the trajectory inclination angle, trajectory deflection angle, and velocity inclination angle, respectively; θ_0, φ_0, and A_0 denote the initial latitude, longitude, and launch azimuth, respectively.

2.2. Methodological Framework. The boost-phase trajectory planning method considering NRACs proposed in this paper mainly consists of six parts. ① Polynomial was selected to parameterize the reachable area boundary obtained by the fast calculation method. ② The constraint transformation rules were proposed to calculate the new reachable area boundary parameters under NRACs. ③ DNNs were trained for the relationship mapping between the boost terminal states and the boundary parameters. ④ The initial values of the boost terminal states were obtained by the trained DNNs and the new reachable area boundary parameters. ⑤ Energy equivalence principles were proposed for the optimal boost terminal states under the separation window constraints. ⑥ The hpPM was used to plan the boost-phase trajectory considering path and terminal constraints. Therefore, the methodological framework is shown in Figure 1.

3. Parametric Description of the Reachable Area

3.1. Fast Calculation Method of the Reachable Area. The problem of the reachable area calculation can be decomposed into the issues on the longest ranges from the separation point to the virtual target points, as shown in Figure 2. VT $i(i = 1, 2 \cdots n)$ denotes the virtual target points; v_0 is the initial velocity direction of the vehicle; $Fi(i = 1, 2 \cdots n)$ represents the longest ground projection points under the energy management conditions, i.e., the farthest arrival points.

When solving the issues on the longest range in the reachable area solution, the earth rotation, oblateness, and gravitational perturbation can be ignored, and the dynamic equations can be simplified based on the quasi-equilibrium glide condition.

$$\begin{cases} \dot{\theta} = \dfrac{V \sin \psi}{\cos \phi}, \\ \dot{\phi} = V \cos \psi, \\ \dot{V} = -\dfrac{1}{C_L/C_D} \dfrac{1 - V^2}{\cos \sigma}, \\ \dot{\psi} = \dfrac{1}{V} \left[\left(1 - V^2\right) \tan \sigma + V^2 \sin \psi \tan \phi \right], \end{cases} \tag{5}$$

where C_L and C_D denote the aerodynamic lift coefficient and drag coefficient in the gliding phase, respectively.

The subproblem can be transformed into the following optimal control form:

$$\begin{cases} \min J_s = \min \left\{ -\cos S_f \right\}, \\ \dot{x}_s = f(x_s, u, t), \\ H = \lambda_\theta \dot{\theta} + \lambda_\phi \dot{\phi} + \lambda_V \dot{V} + \lambda_\psi \dot{\psi}, \\ \dot{\lambda} = -\dfrac{\partial H}{\partial x_s} \dfrac{\partial H}{\partial u} = 0, \end{cases} \tag{6}$$

where S_f denotes the range; J_s denotes the performance index; $x_s = [\theta, \phi, V, \psi]'$ denotes the states; $f(\cdot)$ denotes the right end term of the system differential equations; λ_θ, λ_ϕ, λ_V, and λ_ψ represent the corresponding covariate variables, respectively; H is Hamiltonian. The pitch angle σ is the only control variable when the attack profile $\alpha = \alpha(V)$ is given in segments.

Since the Hamiltonian function does not consider time, the analytical form of the optimal control solution can be obtained by using the control equation and the costate Equation (12):

$$\begin{cases} \eta_1 = \sin \chi \eta_2 = -\eta_1 \tan \Phi_T \eta_3 = \cos \chi, \\ \tan \sigma = \dfrac{\left(1 - 1/V^2\right)\left(\eta_1 \sin \phi + \left(\eta_2 \cos \theta + \eta_3 \sin \theta\right) \cos \phi\right)}{\eta_1 \cos \phi \sin \psi + \eta_2 (\sin \theta \cos \psi - \cos \theta \sin \psi \sin \phi) - \eta_3 (\sin \theta \sin \phi \sin \psi + \cos \theta \cos \psi)} \\ \sin \chi \sin \phi_f - \sin \chi \tan \Phi_T \cos \left(\theta_f - \Theta_T\right) \cos \phi_f + \cos \chi \sin \left(\theta_f - \Theta_T\right) \cos \phi_f = 0, \end{cases} \tag{7}$$

where Θ_T and Φ_T denote the latitude and longitude of the virtual target point, respectively; θ_f and ϕ_f denote the terminal latitude and longitude of the gliding phase, respectively.

The optimal control solution satisfying the requirements of the longest range can be found by iterating the univariate χ. The reachable area boundary can be obtained by connect-

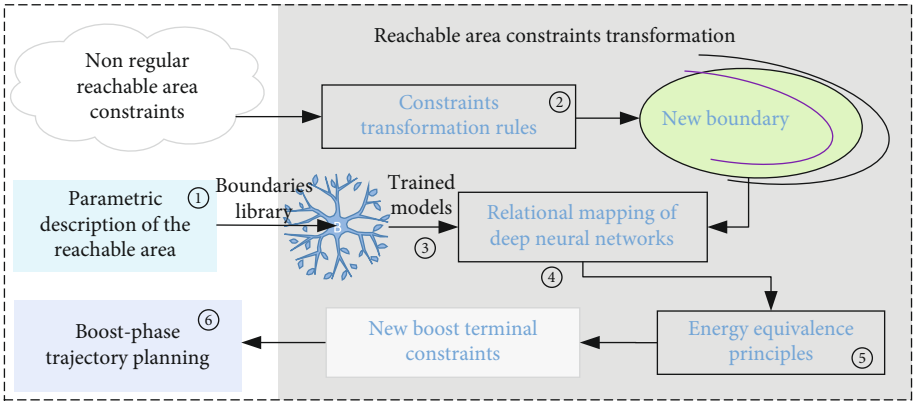

Figure 1: Methodological framework.

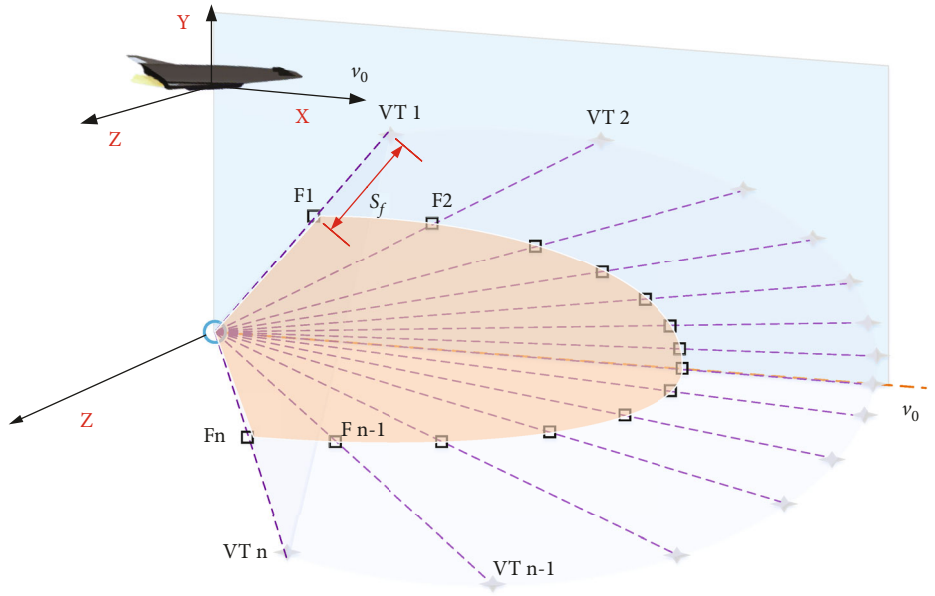

Figure 2: Schematic diagram of the vehicle's reachable area.

Table 1: Nominal states.

Item	Value (unit)
Height	70 km
Velocity	5000 m/s
Flight path angle	-1°
Heading angle	90°

Table 2: List of initial state deviations.

Item	Maximum value (unit)
Height deviation	±20 km
Velocity deviation	±200 m/s
Flight path angle deviation	±5°

ing the farthest arrival point obtained by solving the issues on the longest range.

The nominal initial states and deviations are designed as shown in Tables 1 and 2.

The reachable area shown in Figure 3 can be obtained by the fast calculation method by superimposing the normal distribution deviation shown in Table 2 on the nominal initial states. At the same time, the coordinate data of the reachable area is normalized to facilitate the fitting calculation of large data samples.

3.2. Parametric Description. Considering that the boundary of the reachable area is a continuous closed curve connected by a series of boundary points, it can be described by curve parameters. Suppose that the boundary of the reachable area can be defined in the form of the following curve:

$$y = a + b_1 x + b_2 x^2 + \cdots + c \sin(wx) + de^{-\xi x} + \eta e^{-((x-\delta_1)/\delta_2)^2}. \tag{8}$$

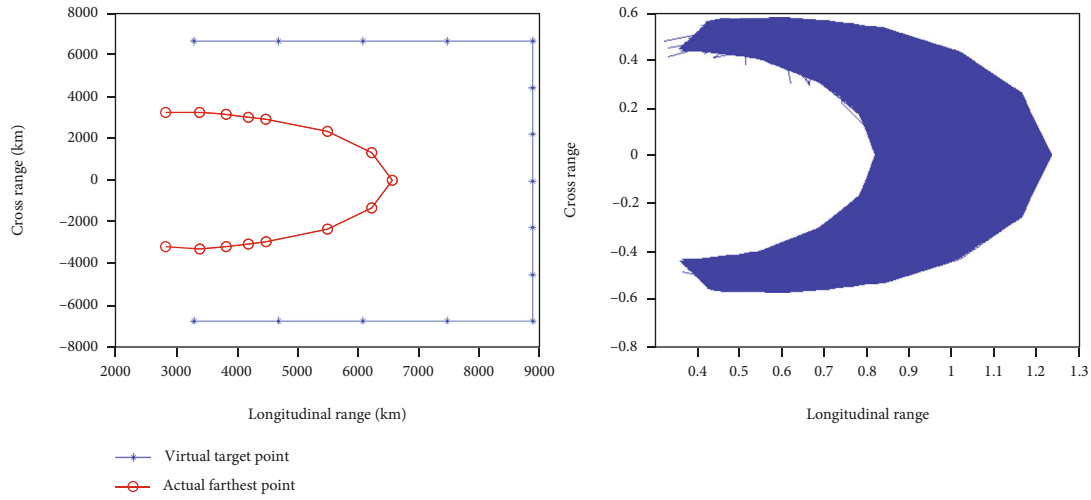

Figure 3: The reachable area under nominal conditions.

Table 3: List of fitting results of different forms of curves.

Order	Curve form	R-square	RMSE
1	$y = a + b_1x + b_2x^2$	0.93560	0.04251
2	$y = a + b_1x + b_2x^2 + b_3x^3$	0.93560	0.04440
3	$y = a + b_2x^2$	0.93560	0.04084
4	$y = a + b_2x^2 + c\sin(wx)$	0.93560	0.04656
5	$y = a + b_2x^2 + de^{-\xi x}$	0.93560	0.04440
6	$y = a + b_2x^2 + \eta e^{-((x-\delta_1)/\delta_2)^2}$	0.93230	0.04552

The least-square method is used to select the best fitting curves in different forms. The fitting results of different forms of curves are shown in Table 3.

The fitting results show that too much increase in the order and complexity of the curve will increase the fitting deviation. Therefore, the curve form corresponding to No. 3 is finally selected as the parametric description form of the reachable area boundary. The results after parameter normalization are shown in Figure 4.

4. Reachable Area Constraint Transformation

4.1. Constraint Transformation Rules. This section describes the method to transform NRACs to generate new coverage envelopes about the reachable area. As shown in Figure 5, the projection of the boost terminal point on the ground is the origin O, and the coordinate system is established in the horizontal plane, with the axis Ox in the same direction as the projection of the initial velocity direction $\mathbf{v}_0$ on the ground. The original terminal states of the boost phase are (h_0, v_0, γ_0); $x = a_0y^2 + b_0(-y_{\max} \le y \le y_{\max})$ is the reachable area boundary curve generated by (h_0, v_0, γ_0); the nonregular reachable area is Q; the distance from the farthest point in Q to the coordinate origin is R; the angle between l_L and l_R formed by the left and right boundary points of Q and the coordinate origin O is $\Delta\xi$; the centerline of $\Delta\xi$ is the new axis Ox'; the angle between Ox' and Ox is $\Delta\psi_t$; $L_T : x = ay^2 + b$ denotes the new reachable area boundary curve, so the key of the issue is to solve the parameters of L_T.

Whether the original terminal states of the boost phase are appropriate can be judged by the relative position relationship between the boundary points of Q and the boundary of the original reachable area.

$$\begin{cases} \text{Judgment } 1: a_0(R\sin(\Delta\psi_t))^2 + b_0 > R\cos(\Delta\psi_t), \\ \text{Judgment } 2: a_0\left(l_0\sin\left(\Delta\psi_t - \frac{1}{2}\Delta\xi + \Delta\xi\frac{0}{n}\right)\right)^2 + b_0 > l_0\cos\left(\Delta\psi_t - \frac{1}{2}\Delta\xi + \Delta\xi\frac{0}{n}\right), \\ \text{Judgment } 3: a_0\left(l_1\sin\left(\Delta\psi_t - \frac{1}{2}\Delta\xi + \Delta\xi\frac{1}{n}\right)\right)^2 + b_0 > l_0\cos\left(\Delta\psi_t - \frac{1}{2}\Delta\xi + \Delta\xi\frac{1}{n}\right) \\ \cdots \\ \text{Judgment } i: a_0\left(l_{i-2}\sin\left(\Delta\psi_t - \frac{1}{2}\Delta\xi + \Delta\xi\frac{i-2}{n}\right)\right)^2 + b_0 > l_{i-2}\cos\left(\Delta\psi_t - \frac{1}{2}\Delta\xi + \Delta\xi\frac{i-2}{n}\right), \end{cases} \quad (9)$$

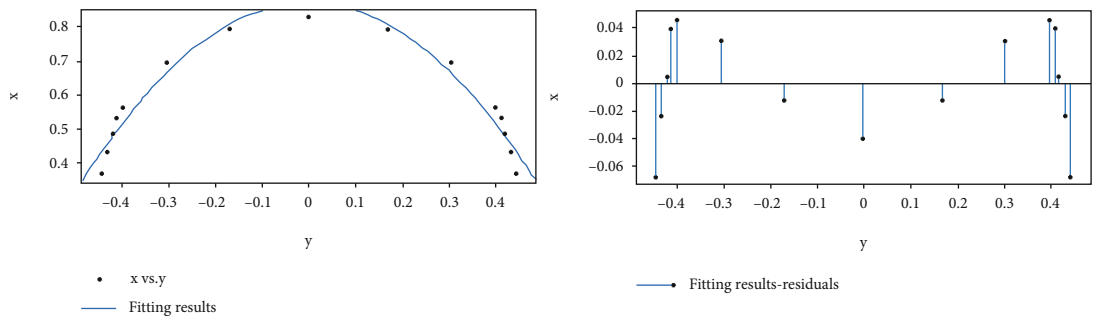

Figure 4: Fitting results of the reachable area under nominal conditions. (Note: x and y denote the normalized longitudinal and cross ranges, respectively).

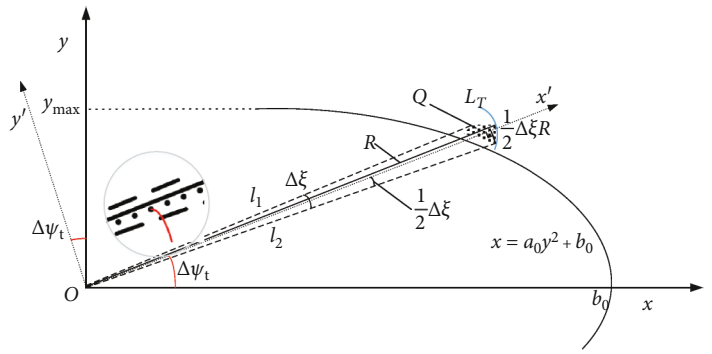

Figure 5: Description of the coverage requirements of the nonregular reachable area.

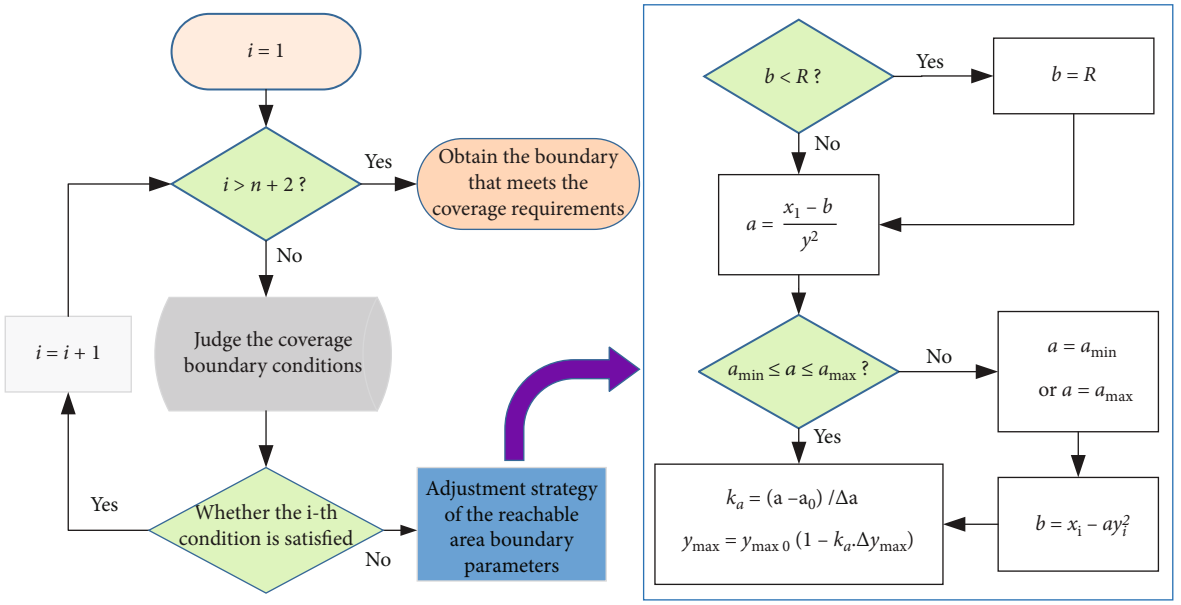

Figure 6: Adjustment strategies for the reachable area boundary parameters.

where n is the number of divisions when judging the boundary for Q; l_i is the distance from the coordinate origin to the i-th boundary judgment point. The $n + 2$ judgment conditions must be satisfied simultaneously to determine whether the original terminal states of the boost phase are appropriate. The number of divisions can be obtained according to the description accuracy of the reachable area and the shape of Q.

When the original terminal states of the boost phase do not meet NRACs, the change of initial heading angle can bring great convenience to the adjustment of the reachable area. However, the reachable area adjusted by the initial

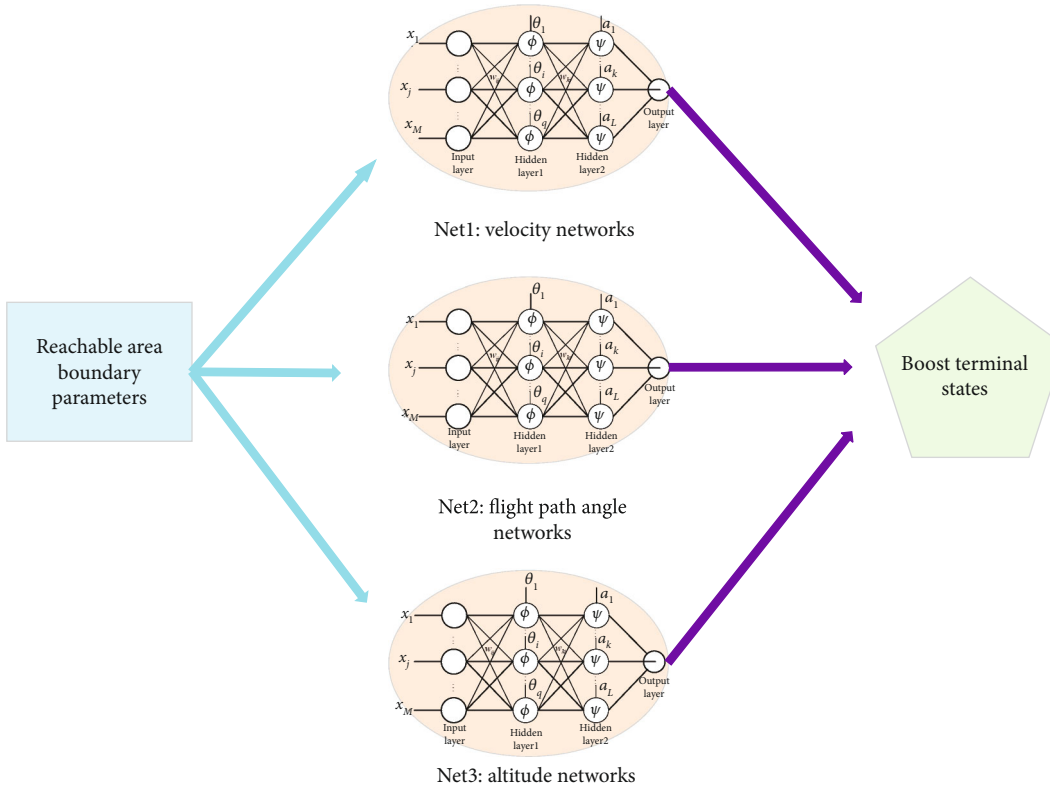

Figure 7: Relational mapping diagram of deep neural networks.

flight direction may still not meet the coverage requirements. Therefore, the judgments need to be reconducted in the new $Ox'y'$-coordinate system.

$$\begin{cases} \text{Judgment } 1: b_0 > R, \\ \text{Judgment } 2: a_0\left(l_0 \sin\left(-\frac{1}{2}\Delta\xi + \Delta\xi\frac{0}{n}\right)\right)^2 + b_0 > l_0 \cos\left(-\frac{1}{2}\Delta\xi + \Delta\xi\frac{0}{n}\right), \\ \text{Judgment } 3: a_0\left(l_1 \sin\left(-\frac{1}{2}\Delta\xi + \Delta\xi\frac{1}{n}\right)\right)^2 + b_0 > l_0 \cos\left(-\frac{1}{2}\Delta\xi + \Delta\xi\frac{1}{n}\right), \\ \cdots \\ \text{Judgment } i: a_0\left(l_{i-2} \sin\left(-\frac{1}{2}\Delta\xi + \Delta\xi\frac{i-2}{n}\right)\right)^2 + b_0 > l_{i-2} \cos\left(-\frac{1}{2}\Delta\xi + \Delta\xi\frac{i-2}{n}\right). \end{cases} \tag{10}$$

When the $n+2$ judgment conditions cannot be satisfied simultaneously, the new boundary parameters can be adjusted and determined according to the range of values of the boundary parameters.

$$\begin{cases} a_{\min} \le a \le a_{\max}, \\ b_{\min} \le b \le b_{\max}, \\ (y_{\max})_{\min} \le y_{\max} \le (y_{\max})_{\max}. \end{cases} \tag{11}$$

As a supporting parameter, the parameter $y_{\max}$ varies inversely and equivalently with the adjustment of a. The adjustment strategies for the three parameters are shown in Figure 6.

4.2. Relational Mapping of Deep Neural Networks. The relationship between the reachable area boundary parameters and the boost terminal states needs to be mapped to obtain effective boost terminal states. The same reachable area may correspond to multiple sets of boost terminal states.

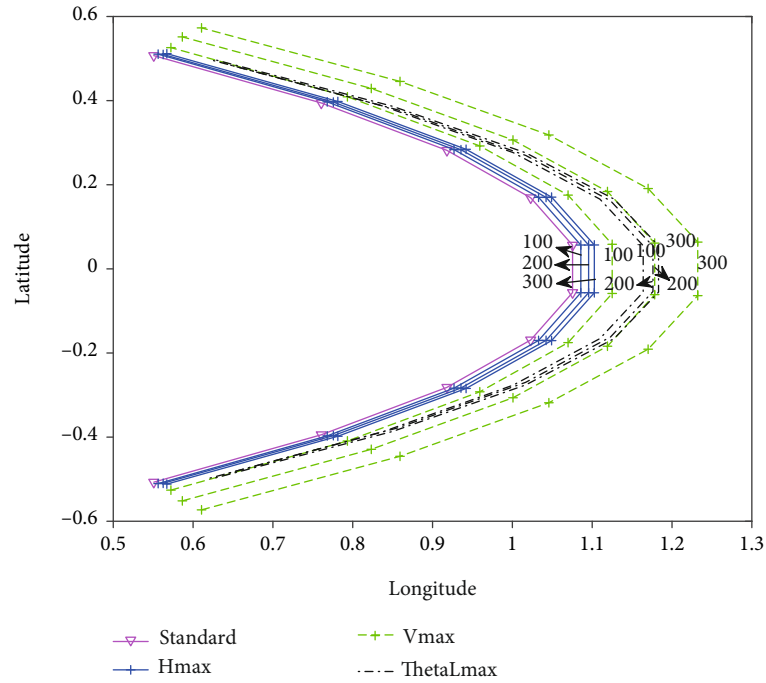

Figure 8: Effect of terminal states of the boost phase on the reachable area.

Table 4: Relationship between boost terminal states and reachable area boundary parameters.

States	States change	Variation of boundary curve parameters
Height (km)	0	$\Delta a = 1.0068719 \times 10^{-9}, \Delta b = 4.7115307 \times 10^{-8}, \Delta y_{max} = 0$
	10.4	$\Delta a = 8.3883981 \times 10^{-3}, \Delta b = 1.0403449 \times 10^{-2}, \Delta y_{max} = 3.3730000 \times 10^{-3}$
	17.3	$\Delta a = 1.0925126 \times 10^{-2}, \Delta b = 2.0196111 \times 10^{-2}, \Delta y_{max} = 2.6560000 \times 10^{-3}$
	23.25	$\Delta a = 5.5262781 \times 10^{-3}, \Delta b = 2.7402044 \times 10^{-2}, \Delta y_{max} = 4.5460000 \times 10^{-3}$
Velocity (m/s)	0	$\Delta a = 1.0068719 \times 10^{-9}, \Delta b = 4.7115307 \times 10^{-8}, \Delta y_{max} = 0$
	69.2	$\Delta a = 4.2817309 \times 10^{-2}, \Delta b = 4.9985394 \times 10^{-2}, \Delta y_{max} = 1.8905000 \times 10^{-2}$
	142	$\Delta a = -9.6140915 \times 10^{-2}, \Delta b = 1.0372763 \times 10^{-1}, \Delta y_{max} = 4.4436000 \times 10^{-2}$
	216.3	$\Delta a = -1.4838703 \times 10^{-1}, \Delta b = 1.5801915 \times 10^{-1}, \Delta y_{max} = 6.5828000 \times 10^{-2}$
Flight path angle (°)	4.25	$\Delta a = 8.9585021 \times 10^{-2}, \Delta b = 6.2255655 \times 10^{-2}, \Delta y_{max} = -3.6950000 \times 10^{-3}$
	6.5	$\Delta a = -1.5504815 \times 10^{-1}, \Delta b = 8.8706775 \times 10^{-2}, \Delta y_{max} = -9.7200000 \times 10^{-3}$
	7.8	$\Delta a = 2.1084387 \times 10^{-1}, \Delta b = 1.0807930 \times 10^{-1}, \Delta y_{max} = -1.0417000 \times 10^{-2}$
	8.9	$\Delta a = 2.1735414 \times 10^{-1}, \Delta b = 1.0080363 \times 10^{-1}, \Delta y_{max} = -2.1716000 \times 10^{-2}$

Table 5: General parameters of the vehicle.

Item		Value (unit)
Boost phase	Initial mass	10000 kg
	Consumption per second	60 kg/s
	Specific impulse	300 s
	Pneumatic reference area	1 m^2
	Fuel mass	5850 kg
Gliding phase	Mass	1000 kg
	Pneumatic reference area	0.5 m^2

However, the reachable area boundary parameters caused by the deviation of the boost terminal states are unique. Therefore, it is possible to construct the mapping relationship to realize the transformation from the reachable area boundary to the terminal state increments of the boost phase. Thus, the networks of altitude, velocity, and flight path angle as shown in Figure 7 are established.

Generally, the neural networks with 1~2 hidden layers can fit the nonlinear smooth mapping with arbitrary accuracy, and the ability of neural networks to describe complex learning can be increased by introducing the third hidden layer [25]. For the training of neural networks with three

Table 6: Mission parameters.

Item	Value (unit)
Air-based launch point	$\theta = 0^\circ, \varphi = 0^\circ$
The initial velocity of the boost phase	$V = 3101$ m/s, $\theta_v = 9.31^\circ$
The initial position of the boost phase	$x = 635000$ m, $y = -3000$ m, $z = 10000$ m
Nominal terminal states of the boost phase	$h = 70$ km, $v = 5000$ m/s, $\gamma = -1^\circ, \psi = 111^\circ$
Control constraints	$-20^\circ \le \alpha \le 20^\circ$, $-10^\circ \le \beta \le 10^\circ$
Control rate constraints	$\lvert\dot{\alpha}\rvert \le 10^\circ$/s, $\lvert\dot{\beta}\rvert \le 5^\circ$/s
Separation window constraints	$\Delta v_{\max} = 100$ m/s, $\Delta\gamma_{\max} = 3^\circ$, $\Delta h_{\max} = 10$ km
Terminal states of the gliding phase	$h_f = 20$ km, $v_f = 1000$ m/s
Required coverage area	$P1 : (54^\circ, 18^\circ), P2 : (59^\circ, 18^\circ), P3 : (56^\circ, 13^\circ), P4 : (52^\circ, 11^\circ)$

Table 7: Disturbances and deviation conditions.

Item		Deviation value	
		Maximum energy	Minimum energy
Initial state deviations	Position (m)	[2000, 2000, 1000]	[-2000, -2000, -1000]
	Velocity (m/s)	[20, 20, 10]	[-20, -20, -10]
Power system deviation	Fuel mass (kg)	50	-50
Environmental disturbances	Resistance coefficient (%)	-15	15
	Lift coefficient (%)	15	-15
	Atmospheric density (%)	-10	10

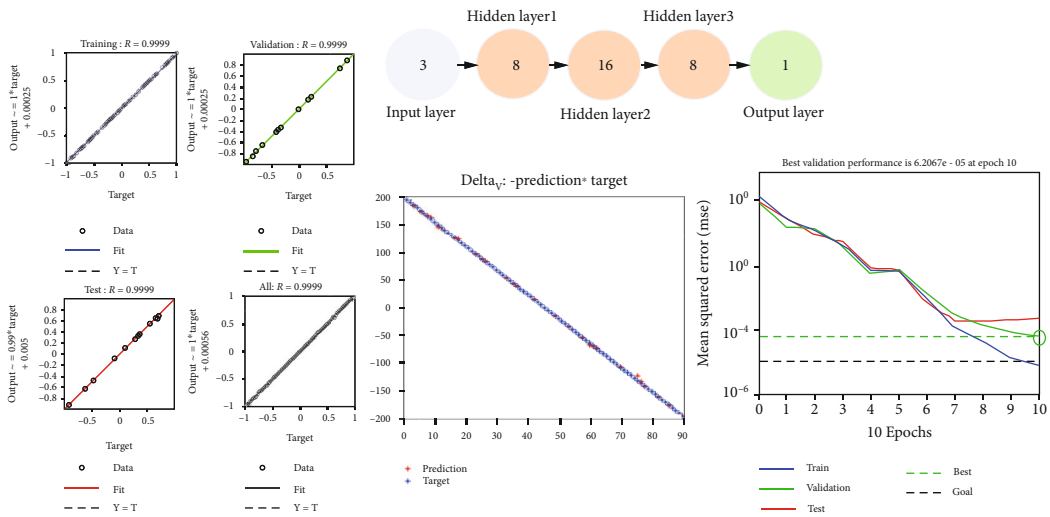

Figure 9: Training results of velocity neural networks.

parameters of the reachable area boundary as input and one terminal state increment of the boost phase as output, the number of hidden layers was set to 3 in this study. For the hyperparameter setting of other hidden layer neural networks, some meaningful manual optimization rules were given in Nielsen's works [26]. In literature [27, 28], an automatic optimization method of hyperparameters using grid search technology was introduced. Therefore, this paper only briefly gives the process of determining the number of hidden layers: firstly, the number of nodes in each hidden layer is set to 2~20; then, the number of hidden layer nodes is increased in turn for network training; finally, the network structure with the least total error on the verification is recorded as the optimal neural network structure.

4.3. Energy Equivalence Principles. It is necessary to adopt the optimal adjustment strategy of the reachable area according to the influence of the boost terminal states considering limited fuel. Under fixed time constraints, the trajectory optimization was carried out with the boost

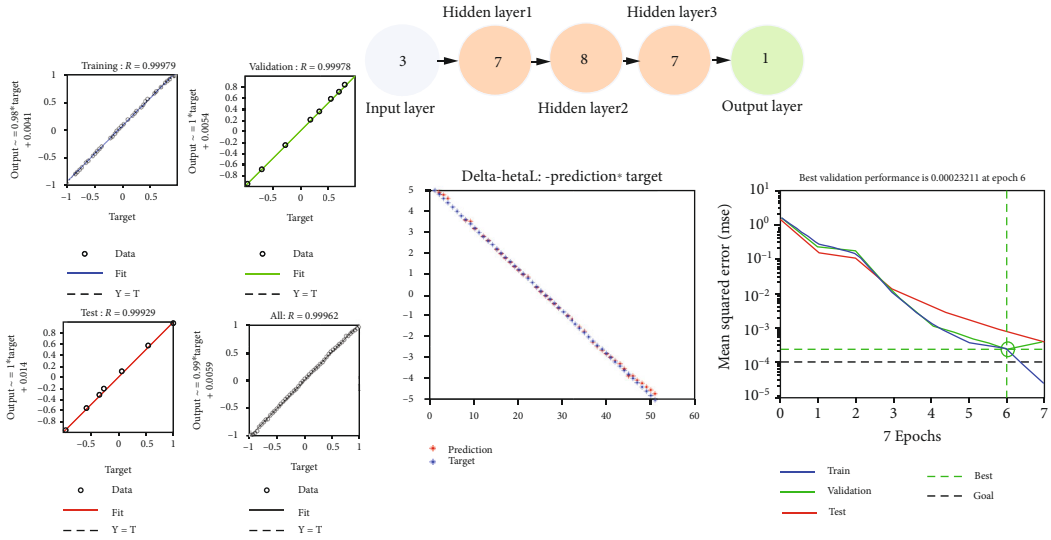

Figure 10: Training results of flight path angle neural networks.

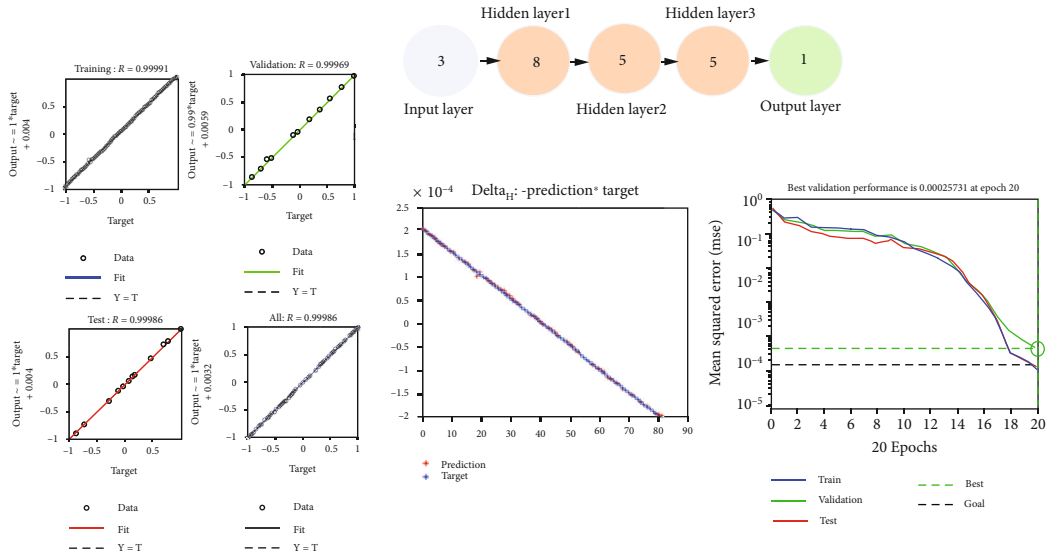

Figure 11: Training results of high neural networks.

Table 8: Parameters of NSGA II.

Item	Value
PopulationSize	200
Generations	80
StallGenLimit	40
CrossoverFraction	0.8
MigrationFraction	0.4
ParetoFraction	0.3

terminal point's altitude, velocity, and flight path angle as performance indexes. By taking the obtained boost terminal states as the initial condition for the glider, the reachable area boundaries under different energy consumption conditions (100 kg, 200 kg, and 300 kg fuel increase, respectively) as shown in Figure 8 are obtained by the method in Section 3.1.

Under the same energy consumption conditions, the reachable area obtained by raising the velocity of the boost terminal was larger than the reachable area obtained by raising the flight path angle of the boost terminal, and both were larger than the reachable area obtained by increasing the height of the boost terminal. Therefore, on the basis of getting the new reachable area boundary parameters, the terminal states of the boost phase can be obtained through DNNs described in Section 4.2. The selection priority of the mapping networks is velocity networks>flight path angle networks>altitude networks.

Although the selection priority can maximize the reachable area, the terminal states of the boost phase must be within a certain limit due to the debris drop point constraints, separation conditions, and the limitation of the

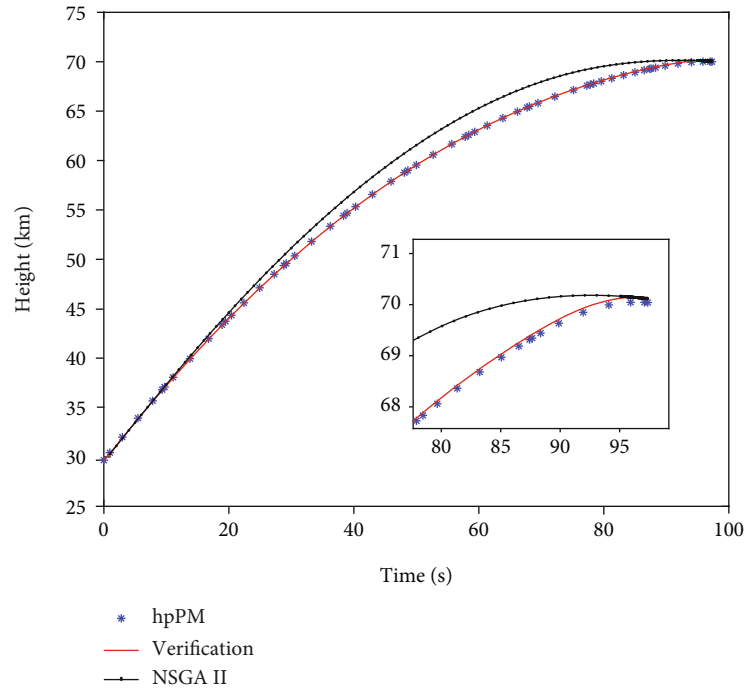

Figure 12: Height.

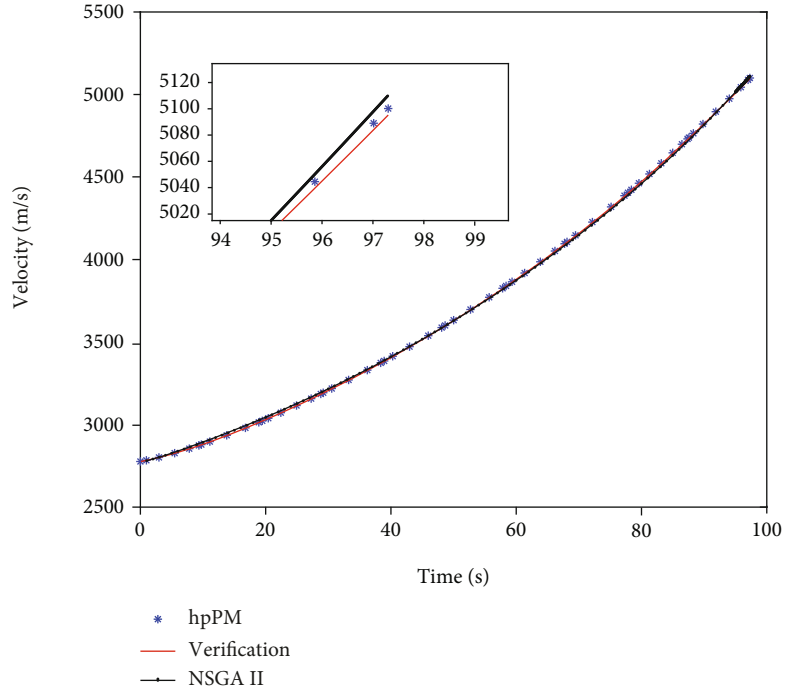

Figure 13: Velocity.

glider's navigation communication window. Assume that the separation window constraints of the booster based on the nominal terminal states are $(\Delta h_{\max}, \Delta v_{\max}, \Delta \gamma_{\max})$. When the boost terminal states obtained by DNN exceed the separation window constraints, the energy equivalence principles are adopted to obtain the new boost terminal states.

The method described in Section 3 can be used to obtain the relationship between the boost terminal states and the reachable area boundary parameters, as shown in Table 4.

The contents of the energy equivalence principles are as follows. ① After the reachable area boundary parameters are obtained by the constraint transformation rules, the velocity networks can be used to obtain the boost terminal velocity

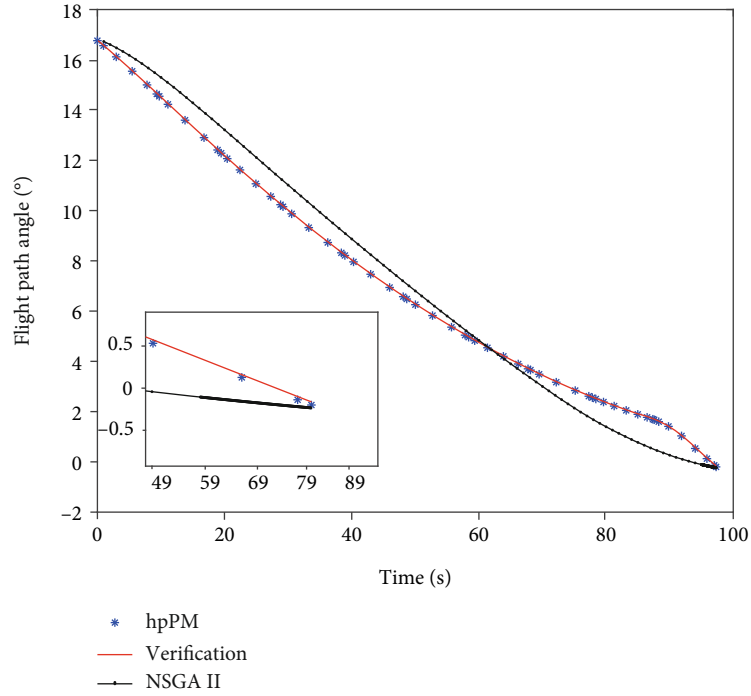

Figure 14: Flight path angle.

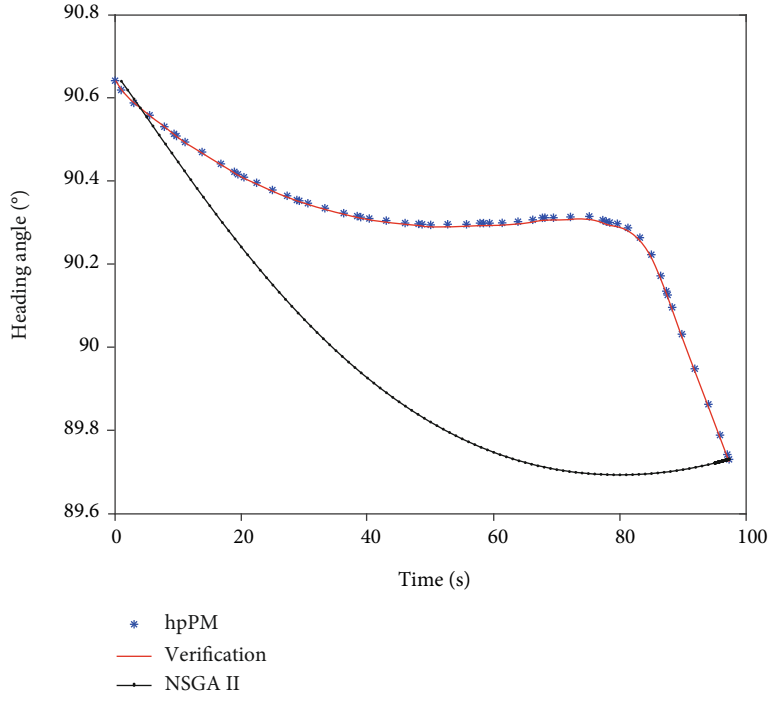

Figure 15: Heading angle.

increment Δv. If $\Delta v \le \Delta v_{\max}$, the final boost terminal state constraints are $(h_0, v_0 + \Delta v, \gamma_0)$; if $\Delta v > \Delta v_{\max}$, proceed to the next step. ② Let $\delta\Delta v = \Delta v - \Delta v_{\max}$ and interpolate Table 4 with $\delta\Delta v$ to obtain the reachable area boundary parameter increment $\Delta(a, b, y_{\max})_{\Delta v}$; then, the flight path angle neural networks can be used to obtain the new boost terminal increment of the flight path angle $\Delta\gamma$. If $\Delta\gamma \le \Delta\gamma_{\max}$, the final boost terminal state constraints are $(h_0, v_0 + \Delta v_{\max}, \gamma_0 + \Delta\gamma)$; if $\Delta\gamma > \Delta\gamma_{\max}$, proceed to the next step. ③ Let $\delta\Delta\gamma = \Delta\gamma - \Delta\gamma_{\max}$ and interpolate Table 4 with $\delta\Delta\gamma$ to obtain the increment of reachable area boundary parameters $\Delta(a, b, y_{\max})_{\Delta\gamma}$; then, the height neural networks are used to

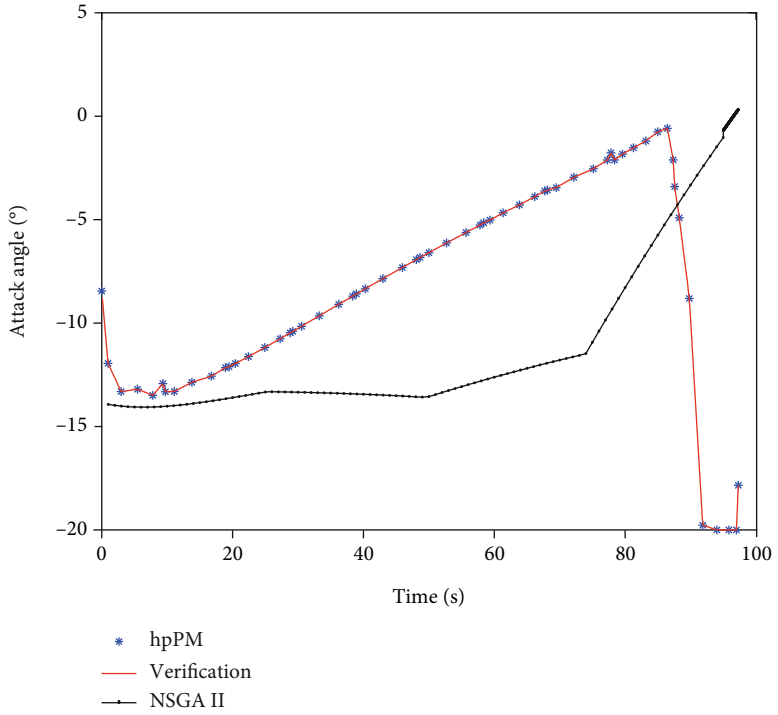

Figure 16: Attack angle.

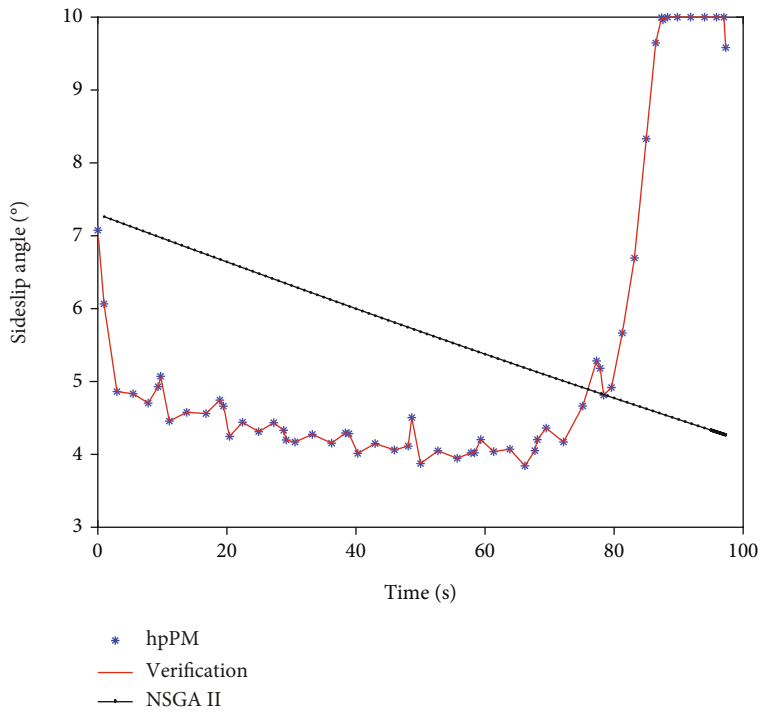

Figure 17: Sideslip angle.

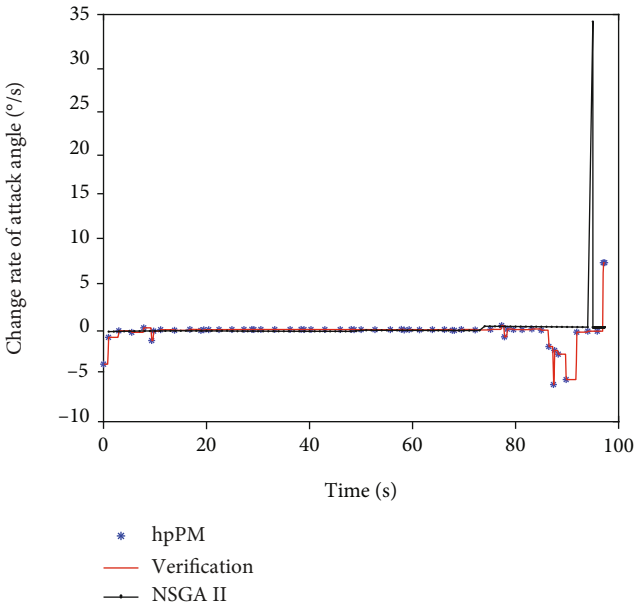

Figure 18: Change rate of attack angle.

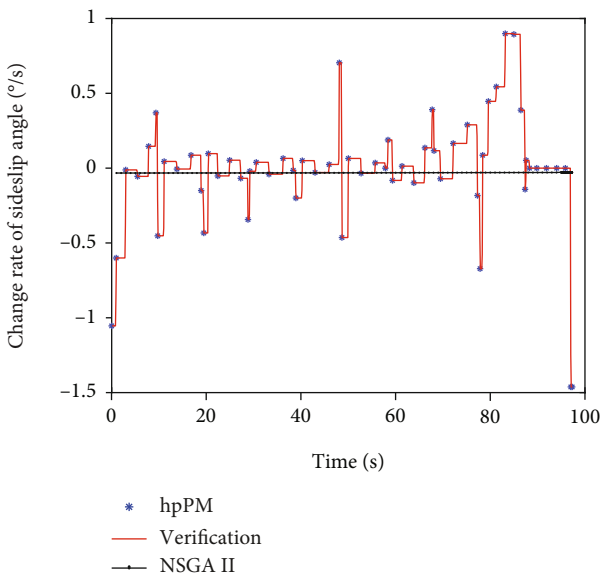

Figure 19: Change rate of sideslip angle.

obtain the new boost terminal height increment Δh. If $\Delta h \le \Delta h_{\max}$, the final boost terminal state constraints are $(h_0 + \Delta h, v_0 + \Delta v_{\max}, \gamma_0 + \Delta\gamma_{\max})$; if $\Delta h > \Delta h_{\max}$, the constraint window is exceeded, and the boost terminal states are set to the maximum separation window constraints $(h_0 + \Delta h_{\max}, v_0 + \Delta v_{\max}, \gamma_0 + \Delta\gamma_{\max})$.

5. Boost-Phase Trajectory Planning

After obtaining the terminal state constraints of the boost phase, the trajectory from the initial point to the new terminal point needs to be replanned. Unlike the trajectory tracking with a known reference trajectory [29], the boost-phase

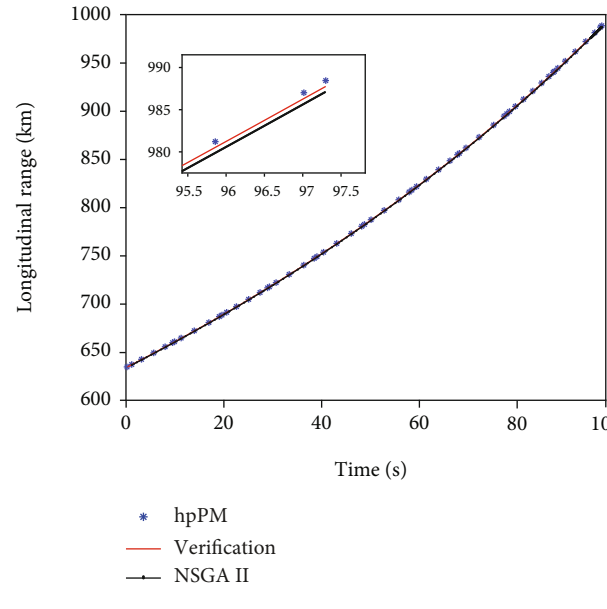

Figure 20: Longitudinal range.

trajectory is replanned under the condition that the initial value is not ideal or there is no reference trajectory in this study. At the same time, the trajectory planning method needs to overcome the impacts of initial deviation and environmental disturbance conditions and needs to meet the process constraints such as states and control and the given terminal states constraints.

The Gaussian pseudospectral method can be used to realize fast and accurate trajectory replanning to meet the requirements of low sensitivity to initial values, good convergence, and high accuracy. Aiming at the "Dimensional Catastrophe" of Jacobian and Hessian matrices and the slow convergence speed when solving nonsmooth problems, the hp-type adaptive finite element method (hp-FEM) is used, which allows the segment length and the order of basis function to change adaptively on the mesh profile at the same time.

By taking the longest range of the boost phase is taken as the performance index, the boost-phase trajectory planning problem is converted into an optimal control problem:

$$\begin{cases} J = -R_e \cdot \arccos\left(\cos\left(\varphi_f\right)\cos\left(\varphi_0\right)\cos\left(\theta_f - \theta_0\right) + \sin\left(\varphi_f\right)\sin\left(\varphi_0\right)\right), \\ \dot{\mathbf{x}}(t) = \mathbf{f}(\mathbf{x}(t), \mathbf{u}(t), t), t \in [t_0, t_f], \\ \phi(\mathbf{x}(t_0), t_0, \mathbf{x}(t_f), t_f) = \mathbf{0}, \\ \mathbf{C}(\mathbf{x}(t), \mathbf{u}(t), t) \le \mathbf{0}, t \in [t_0, t_f], \end{cases} \tag{12}$$

where $\mathbf{x}(t)$ denotes the states; $\mathbf{u}(t)$ denotes the control variables; $\dot{\mathbf{x}}(t) = \mathbf{f}(\mathbf{x}(t), \mathbf{u}(t), t)$ denotes the dynamic equations corresponding to Equation (1); $[t_0, t_f]$ is the time interval; $\phi(\mathbf{x}(t_0), t_0, \mathbf{x}(t_f), t_f)$ denotes the boundary constraints; $\mathbf{C}(\mathbf{x}(t), \mathbf{u}(t), t)$ denotes the path constraints; (θ_0, φ_0) is the latitude and longitude of the launch point; (θ_f, φ_f) is the

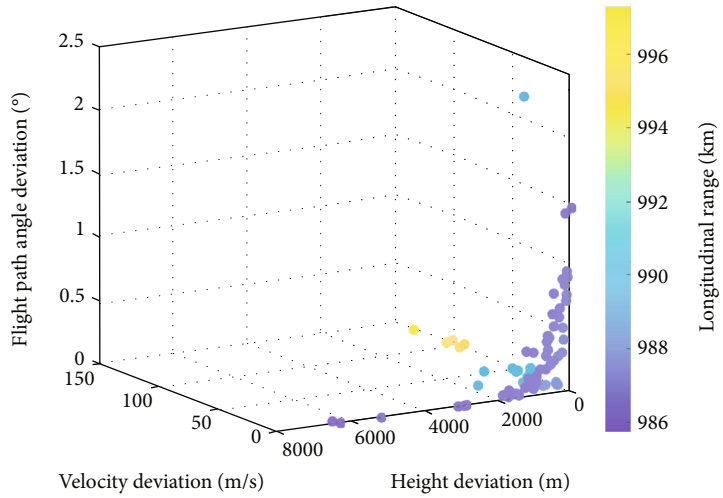

Figure 21: Pareto front.

Table 9: Comparison results.

Item		hpPM	NSGA II
Terminal deviations	Height (m)	0.0	76.0
	Velocity (m/s)	0.0	9.6
	Flight path angle (°)	0.0	-3.4×10^{-2}
	Heading angle (°)	1.0×10^{-3}	-5.0×10^{-3}
Performance index	Maximum range (km)	988.5	987.1
Path constraints	Maximum attack angle (°)	20.0	20.0
	Maximum change rate of attack angle (°/s)	5.8	34.2
	Maximum sideslip angle (°)	10.0	7.3
	Maximum change rate of sideslip angle (°/s)	1.4	3.0×10^{-2}
Timeliness	Calculation time (s)	2.8	318.3

latitude and longitude of the terminal location of the boost phase.

The control variables are the attack angle and sideslip angle:

$$\mathbf{u}(t) = [\alpha, \beta] \tag{13}$$

Boundary constraints are as follows:

$$\begin{cases} h(\mathbf{x}(t_f), t_f) - h_f = 0, \\ v(\mathbf{x}(t_f), t_f) - v_f = 0, \\ \gamma(\mathbf{x}(t_f), t_f) - \gamma_f = 0, \\ \psi(\mathbf{x}(t_f), t_f) - \psi_f = 0, \end{cases} \tag{14}$$

where h_f, v_f, γ_f, and ψ_f denote the terminal altitude, velocity, flight path angle, and heading angle, respectively.

Path constraints are as follows:

$$\begin{cases} \mathbf{x}_{\min} \le \phi(\mathbf{x}(t), t) \le \mathbf{x}_{\max}, \\ \alpha_{\min} \le \alpha \le \alpha_{\max}, \\ |\dot{\alpha}| \le |\dot{\alpha}|_{\max}, \\ \beta_{\min} \le \beta \le \beta_{\max}, \\ \left|\dot{\beta}\right| \le \left|\dot{\beta}\right|_{\max}. \end{cases} \tag{15}$$

The time, states, and control variables must be transformed and discretized. $\mathbf{X}(\tau)$ denotes the discretized states, and $\mathbf{U}(\tau)$ denotes the control variables. The time interval $[t_0, t_f]$ is converted into [-1,1].

$$\tau = \frac{2t}{t_f - t_0} - \frac{t_f + t_0}{t_f - t_0}. \tag{16}$$

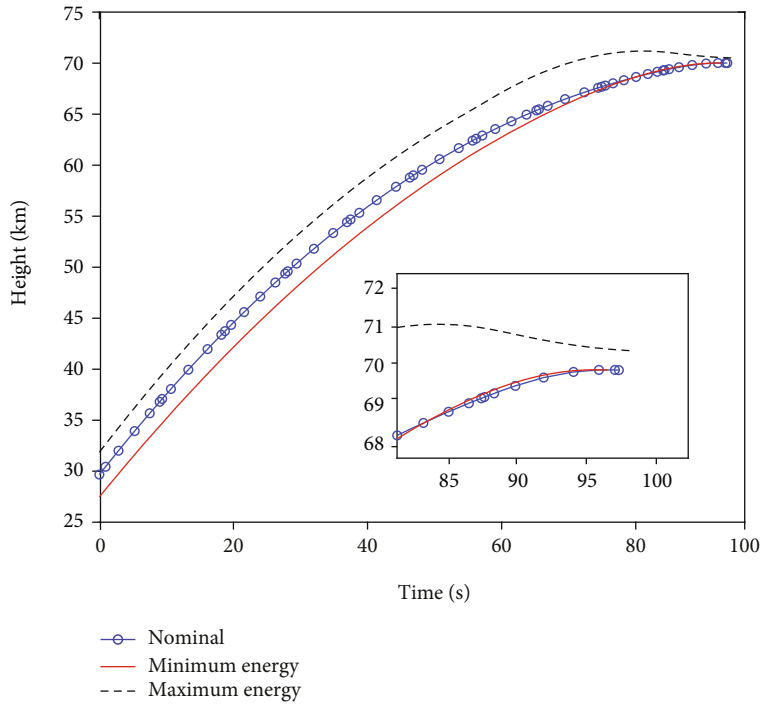

Figure 22: Height.

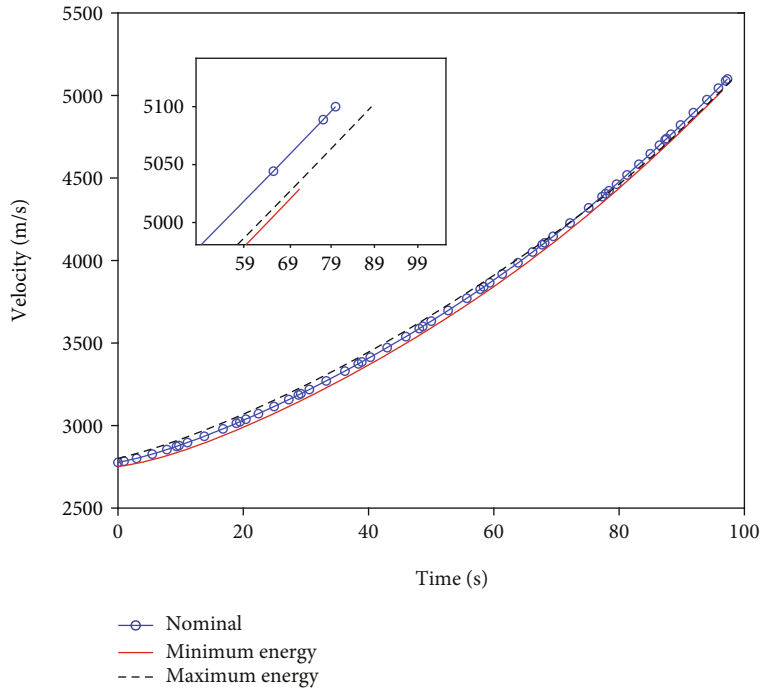

Figure 23: Velocity.

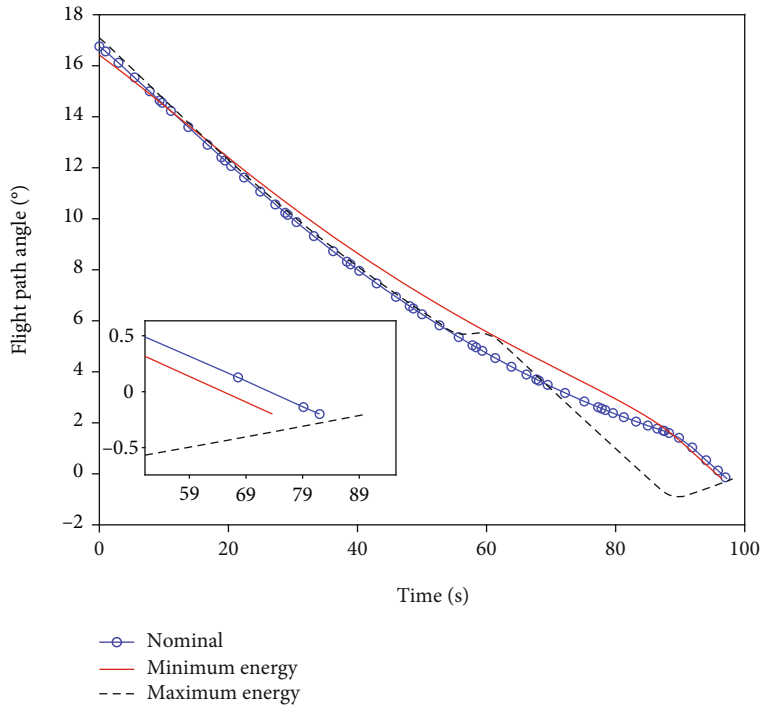

Figure 24: Flight path angle.

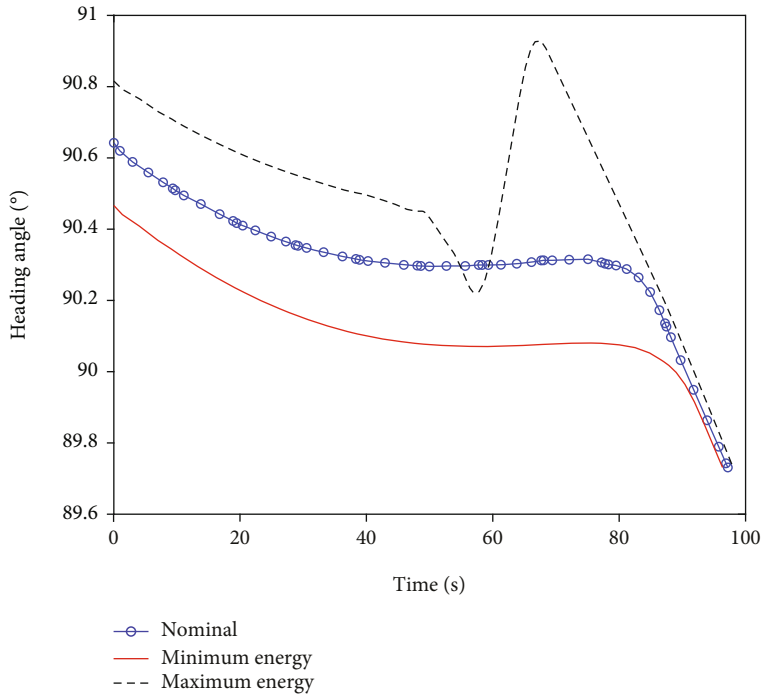

Figure 25: Heading angle.

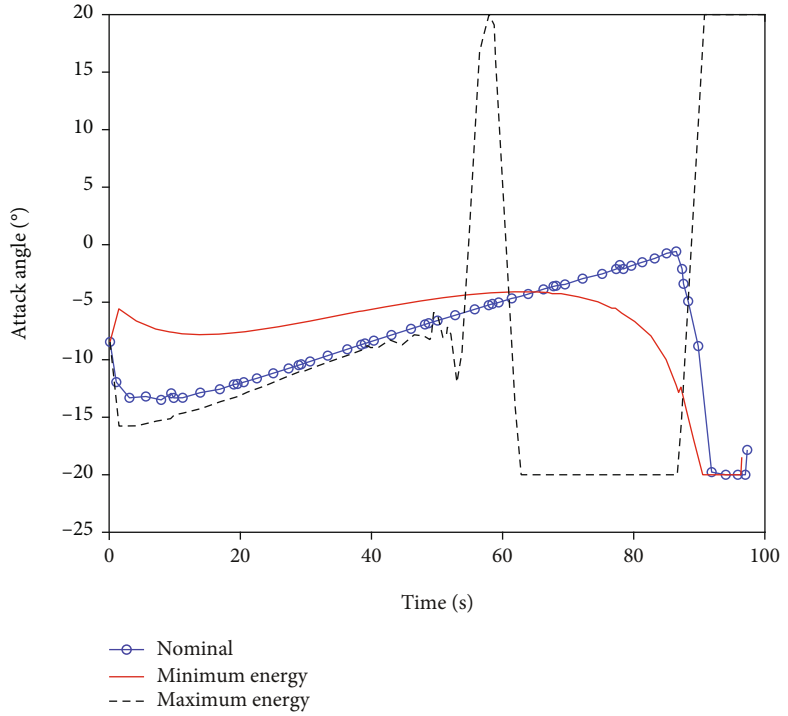

Figure 26: Attack angle.

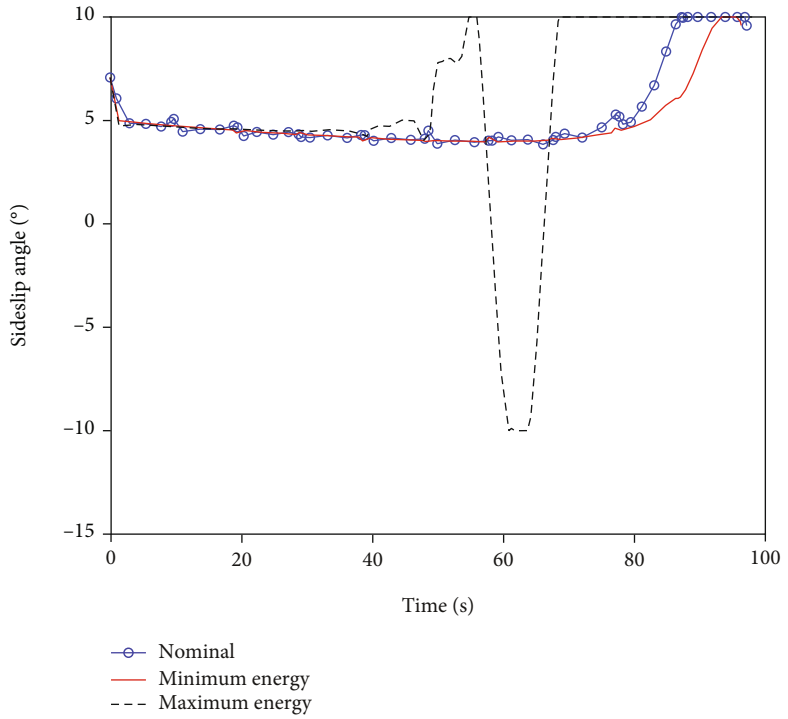

Figure 27: Sideslip angle.

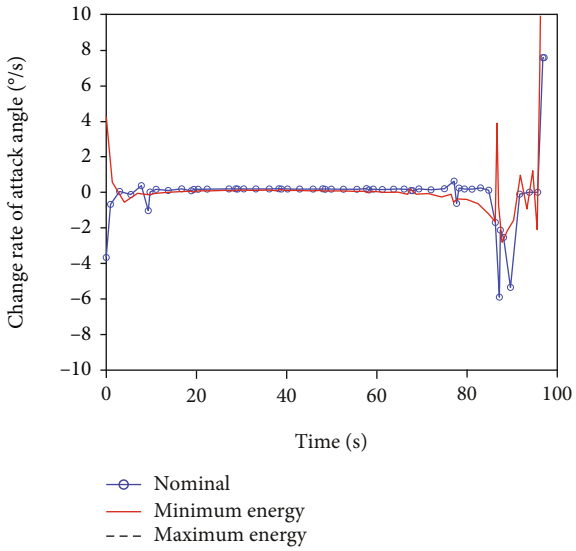

Figure 28: Change rate of attack angle.

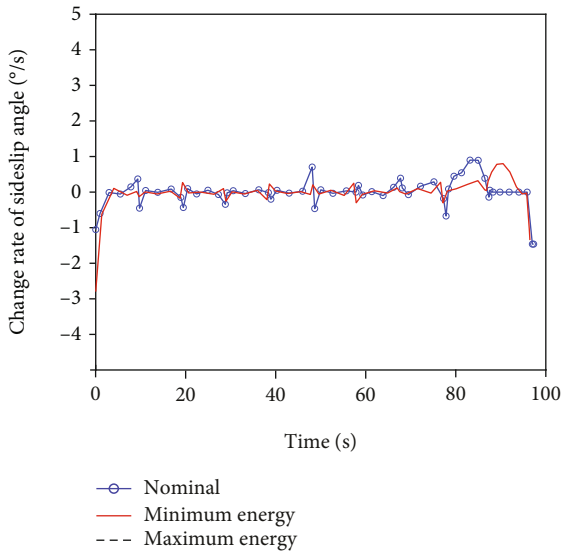

Figure 29: Change rate of sideslip angle.

Taking K-th Legendre-Gauss points $\{\tau_1,\cdots,\tau_K\}$ and $\tau_0 = -1$ as nodes, the $K+1$-th Lagrange interpolation polynomials are formed as basis functions to approximate the states.

$$\begin{cases} \mathbf{x}(\tau) \approx \mathbf{X}(\tau) = \sum_{i=0}^{K} L_i(\tau)\mathbf{x}(\tau_i) \\ L_i(\tau) = \prod_{j=0,j\neq i}^{K} \dfrac{\tau-\tau_j}{\tau_i-\tau_j}. \end{cases}, \tag{17}$$

The approximation of control variables are as follows:

$$\begin{cases} \mathbf{u}(\tau) \approx \mathbf{U}(\tau) = \sum_{i=1}^{K} \tilde{L}_i(\tau)\mathbf{u}(\tau_i), \\ \tilde{L}_i(\tau) = \prod_{j=1,j\neq i}^{K} \dfrac{\tau-\tau_j}{\tau_i-\tau_j}. \end{cases} \tag{18}$$

Furthermore, the kinetic differential equations can be transformed into algebraic constraints.

$$\begin{cases} \dot{\mathbf{x}}(\tau_k) \approx \dot{\mathbf{X}}(\tau_k) = \sum_{i=0}^{K} \dot{L}_i(\tau_k)\mathbf{X}(\tau_i) = \sum_{i=0}^{K} D_{ki}(\tau_k)\mathbf{X}(\tau_i), \\ \sum_{i=0}^{K} D_{ki}(\tau_k)\mathbf{X}(\tau_i) - \dfrac{t_f - t_0}{2}\mathbf{f}(\mathbf{X}(\tau_k), \mathbf{U}(\tau_k), \tau_k; t_0, t_f) = \mathbf{0}, (k = 1,\cdots,K), \end{cases} \tag{19}$$

where D_{ki} is the differential matrix derived from the Legendre polynomial; $P_K(\tau)$ is the root of the K-th Legendre polynomial [20].

$$\begin{cases} D_{ki} = \dot{L}_i(\tau_k) = \begin{cases} \dfrac{(1+\tau_k)\dot{P}_K(\tau_k) + P_K(\tau_k)}{(\tau_k-\tau_i)\left[(1+\tau_i)\dot{P}_K(\tau_i) + P_K(\tau_i)\right]}, i \neq k, \\ \dfrac{(1+\tau_i)\ddot{P}_K(\tau_i) + 2\dot{P}_K(\tau_i)}{2\left[(1+\tau_i)\dot{P}_K(\tau_i) + P_K(\tau_i)\right]}, i = k, \end{cases} \\ P_K(\tau) = \dfrac{1}{2^K K!}\dfrac{d^K}{d\tau^K}\left[\left(\tau^2-1\right)^K\right]. \end{cases} \tag{20}$$

Discrete approximation of path constraints are as follows:

$$\begin{cases} \mathbf{x}_{\min} \leq \mathbf{X}(\tau) \leq \mathbf{x}_{\max}, \\ [\alpha_{\min}; \beta_{\min}] \leq \mathbf{U}(\tau) \leq [\alpha_{\max}; \beta_{\max}], \\ \left|\dot{\mathbf{U}}(\tau_j)\right| = \left|\sum_{i=1}^{K} \dot{\tilde{L}}_i(\tau_j)\mathbf{U}(\tau_i)\right| \leq \left[|\dot{\alpha}|_{\max}; \left|\dot{\beta}\right|_{\max}\right]. \end{cases} \tag{21}$$

Discrete approximation of boundary constraints are as follows:

$$\begin{cases} h\left(\mathbf{X}(\tau_f), \tau_f\right) - h_f = 0, \\ v\left(\mathbf{X}(\tau_f), \tau_f\right) - v_f = 0, \\ \gamma\left(\mathbf{X}(\tau_f), \tau_f\right) - \gamma_f = 0, \\ \psi\left(\mathbf{X}(\tau_f), \tau_f\right) - \psi_f = 0. \end{cases} \tag{22}$$

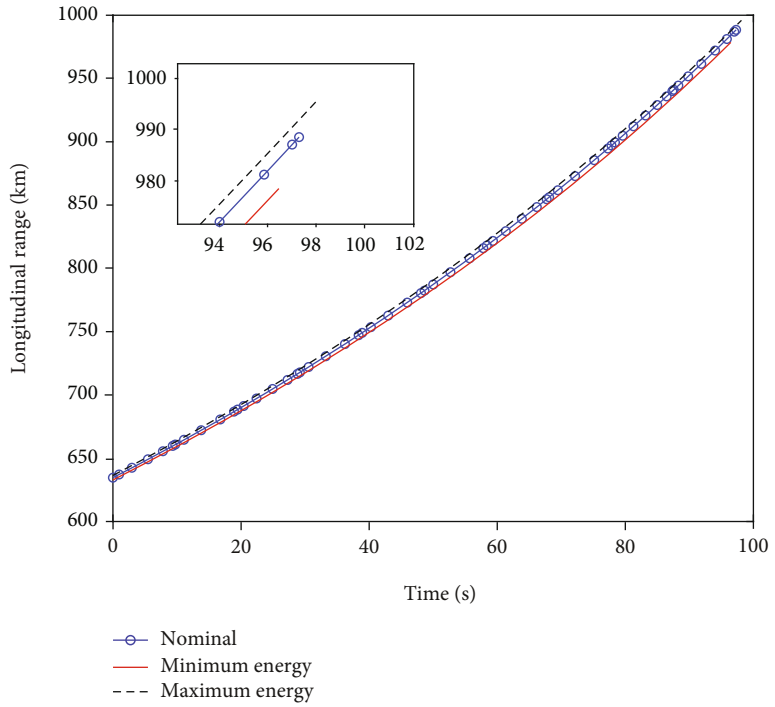

Figure 30: Longitudinal range.

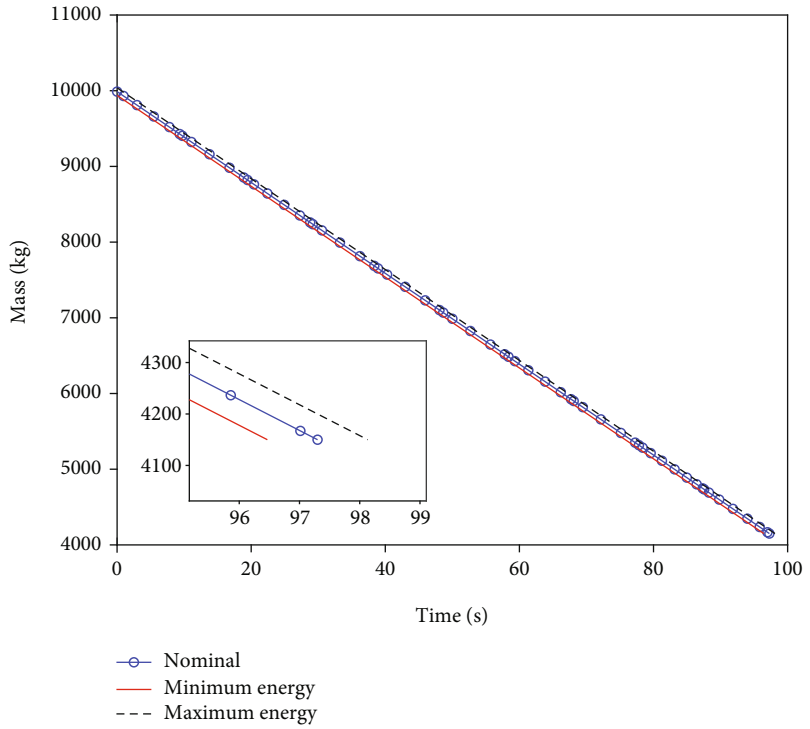

Figure 31: Mass.

Table 10: Results of model uncertainty and disturbances.

Item		Maximum energy	Minimum energy
Terminal deviation	Height (m)	500.0	0.0
	Velocity (m/s)	0.0	-71.0
	Flight path angle (°)	0.0	0.0
	Heading angle (°)	0.0	0.0
Performance index	Maximum range (km)	996.0	978.5
Path constraints	Maximum attack angle (°)	20.0	20.0
	Maximum change rate of attack angle (°/s)	10.0	10.0
	Maximum sideslip angle (°)	10.0	10.0
	Maximum change rate of sideslip angle (°/s)	5.0	2.8
Timeliness	Calculation time (s)	8.6	14.9

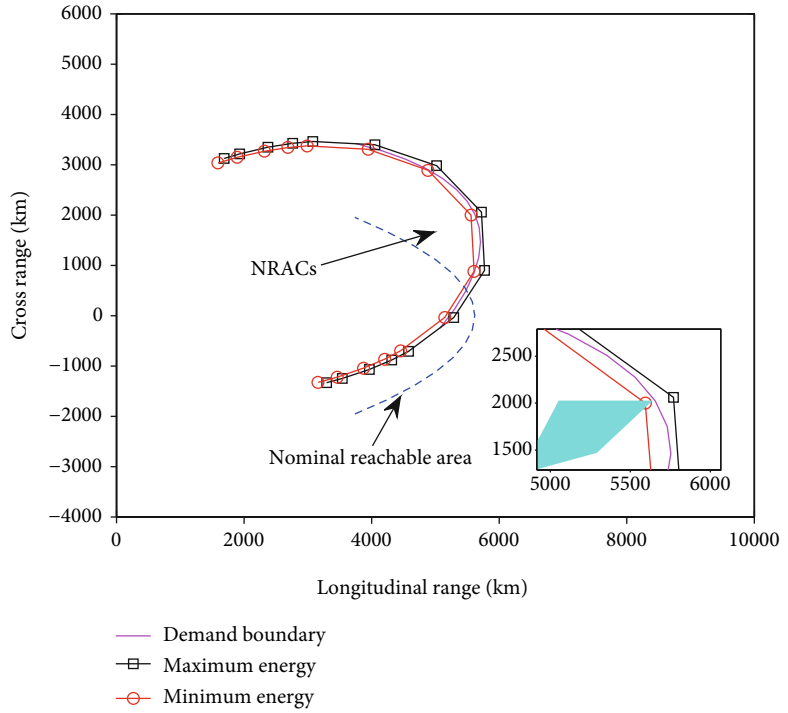

Figure 32: Comparison of the reachable area.

Since the terminal states are not included in the state approximation, a discrete approximation can be performed using Gaussian integration to satisfy the dynamics constraints.

$$\begin{cases} \mathbf{X}(\tau_f) - \mathbf{X}(\tau_0) - \dfrac{t_f - t_0}{2} \displaystyle\sum_{k=1}^{K} w_k \mathbf{f}\left(\mathbf{X}(\tau_k), \mathbf{U}(\tau_k), \tau_k; t_0, t_f\right) = \mathbf{0}, \\ w_k = \displaystyle\int_{-1}^{1} \tilde{L}_k(\tau) d\tau = \dfrac{2}{\left(1 - \tau_k^2\right)\left[\dot{P}_K(\tau_k)\right]^2}. \end{cases} \tag{23}$$

The optimal control problem has been transformed into a discrete nonlinear programming problem, which can be solved using the large-scale sequential quadratic programming-based SNOPT solver.

There have been a great number of research achievements on using the hp-adaptive pseudospectral method to solve the trajectory planning problem [30–32]. The convergence of the Gaussian pseudospectral method has been studied and described in reference [33]. Therefore, this paper will not repeat this part but only discuss the convergence range of the deviation conditions in the simulation section.

6. Simulation and Analysis

6.1. Simulation Settings. The simulation configuration is Intel (R) Core (TM) i7-10510U. The general parameters of the vehicle, mission parameters, disturbances, and deviation conditions required for the simulation are given in Tables 5–7.

6.2. Simulation Results

(1) Training results of deep neural networks

Three different DNNs were trained using the parameterized reachable area boundary library in Section 3.2 as the samples. From the single hidden layer network structure of three neurons, the depth and breadth of neural network are gradually increased until the accuracy requirements are met. The training, verification, and test results are shown in Figures 9–11.

The simulation results show that all three deep neural networks have achieved convergence, with training and testing accuracy higher than 99%. The generated demand reachable area boundary parameter increments are $\Delta a = 0, \Delta b = 0.055, \Delta y_{\max} = 0$ based on the previous geometric relations.

(2) Simulation of boost-phase trajectory planning

To verify the effectiveness of the proposed trajectory planning method and analyze the algorithm's performance, NSGA II as a widely used evolutionary algorithm was used in simulation experiments for comparison. The principle of NSGA II is referred to in [34].

Optimization objectives

$$\begin{cases} J_{N1} = \Delta h_f, \\ J_{N2} = \Delta v_f, \\ J_{N3} = \Delta \gamma_f, \\ J_{N4} = \Delta \psi_f, \\ J_{N5} = -L_{\text{range}}, \end{cases} \tag{24}$$

where Δh_f, Δv_f, $\Delta \gamma_f$, and $\Delta \psi_f$ are the terminal states deviations; L_{range} denotes the terminal range.

Control variables

$$\begin{cases} u_{Ni} = \alpha_{Ni}, i = 1, 2, \cdots, 5, \\ u_{N6} = \dot{\beta}_N, \end{cases} \tag{25}$$

where α_{Ni} denotes i-th of the attack angle at linear interpolation node; $\dot{\beta}_N$ denotes the change rate of sideslip angle.

Constraints

$$\begin{cases} -20^\circ \le u_{Ni} \le 20^\circ, i = 1, 2, \cdots, 5, \\ -5^\circ/s \le u_{Ni} \le 5^\circ/\text{s}, i = 6. \end{cases} \tag{26}$$

Other main parameters are shown in Table 8.

The terminal constraints of the boost phase obtained by using neural networks are $\Delta v = 100$m/s, $\Delta \gamma = 0.8^\circ$, $\Delta h = 0$km , $\Delta \psi = -21.3^\circ$. "hpPM" represents the planning result of the hp-adaptive pseudospectral method, "verification" denotes the integral verification result of the hp-adaptive pseudospectral method, and " NSGA II" represents the planning result of the improved nondominated sorting genetic algorithm. The trajectory planning curves are shown in Figures 12–21, and the comparison results of two methods are shown in Table 9.

The results show that ① the boost-phase flight trajectory obtained by the hpPM that met the requirements of dynamic integration verification; ② the terminal planning accuracy of hpPM was higher than that of NSGA II; ③ the trajectory obtained by hpPM had a larger range than that obtained by NSGA II; ④ the change rate of control angle planned by hpPM was more stable than that by NSGA II in longitudinal profile; the control angle and the change rate of control angle were the same in transverse profile; ⑤ the timeliness of hpPM was significantly better than that of NSGA II.

(3) Influence of disturbances and deviations

Due to the influence of NRACs, the boost-phase trajectory planning with fixed working time has been a challenge. To analyze the impacts of initial state deviations, power system deviation, and environmental disturbances on hpPM, it is necessary to conduct simulation experiments under the limit energy deviation as shown in Table 7. The trajectory planning curves are shown in Figures 22–31, and the results of model uncertainty and disturbances are shown in Table 10.

Due to limited fuel, the adjustment ability of the boost-glide vehicle is limited. Therefore, a limited energy deviation of trajectory planning failure is of great importance. The minimum energy deviation will seriously reduce the flight maneuverability, making the boost-glide vehicle barely reach the designated mission point with the loss of working performance; the maximum energy deviation will make the boost-glide vehicle produce excess flight maneuverability, leading to a large oscillation of attitude angle and instability of flight.

The results show that ① for the maximum energy deviation, the velocity, flight path angle, and heading angle of boost-glide vehicle met the terminal indexes, but the altitude and range were greater than the nominal case, and an over large change rate of control angle was produced. If the magnitude of energy deviations continued to increase, the boost-glide vehicle would lose stability easily or exceed the separation window constraint; ② for the minimum energy deviation, the altitude, flight path angle, and heading angle of the boost-glide vehicle fully met the terminal indexes, but the velocity and range were less than the nominal case. If the magnitude of energy deviations continued to increase, the reachable area of the boost-glide vehicle would be seriously reduced. Therefore, the disturbances and deviations listed in Table 7 can be considered as the failure range of the trajectory planned by hpPM under the mission specified in Table 6.

(4) The verification simulation of the reachable area

After obtaining the deviations of the range, height, and velocity of the boost terminal point, the distribution of reachable area can be calculated, and the effectiveness of the proposed trajectory planning method considering

NRACs can be further analyzed. In the comparison of reachable area distribution, "nominal reachable area" refers to the maneuvering range of the boost-glider vehicle without any adjustments; "demand boundary" refers to the maneuvering range meeting NRACs obtained by the constraint transformation rules; "maximum/minimum energy" represents the maneuvering range under the influence of disturbances and deviations. The results are shown in Figure 32.

The results show that ① the nominal reachable area could not meet the requirements of NRACs, but the demand boundary transformed by the method proposed in this paper completely covered the area specified by NRACs; ② the actual maneuvering range of the boost-glide vehicle still met NRACs under the influence of disturbances and deviations; ③ the average deviation between the actual reachable area boundary and the demand boundary under the limit energy deviation was 3.9%. The above results indicated that the proposed trajectory planning method considering NRACs was sufficiently capable of adjusting the reachable area and had high trajectory planning accuracy and good deviation adaptability.

7. Conclusion

Aiming at the boost-phase trajectory planning under NRACs, this paper studies the parametric description of the reachable area, the reachable area constraint transformation, and the boost-phase trajectory planning. The NRACs were successfully transformed into the terminal state constraints of the boost phase, and the hpPM was used to complete the trajectory planning. The main conclusions are as follows.

(1) The reachable area boundary of the boost-glide vehicle can be described and represented in a simple parametric form. The quadratic form is a feasible solution considering the accuracy and parameter complexity

(2) There is a clear relationship between the reachable area boundary described by parameterization and the boost terminal state change. The DNNs can be used for model learning and parameter mapping, with accuracy of model training and testing greater than 99%. In addition, the changes of boost terminal states pose a significant influence on the reachable area, that is, the influence of velocity was greater than that of flight path angle, and the influence of altitude is the most insignificant

(3) Using the constraint transformation rules, it is possible to quickly determine the reachable area boundary parameters that meet NRACs after changing the initial flight direction of the boost-glide vehicle through the air-based launch mode or the promotion of the front stage

(4) Based on the deep neural networks model and the energy equivalence principles, the appropriate boost terminal states under the separation window constraints can be obtained

(5) The boost-phase trajectory planning method based on the hpPM has good timeliness, high planning accuracy, and strong deviation adaptability

Since this paper focuses on the boost-phase trajectory planning method considering NRACs, the determination of the reachable area of the boost-glide vehicle is mainly depended on the fast calculation method described in Section 3.1 in spite of the influences of the deviations and disturbances of the gliding phase. Future research will focus on the influences of combined deviations in different stages.

Data Availability

The image data used to support the findings of this study are available from the corresponding author upon request.

Conflicts of Interest

The authors declare that there is no conflict of interest regarding the publication of this paper.

Acknowledgments

This study was supported by the open Fund of National Defense Key Discipline Laboratory of Micro-Spacecraft Technology (Grant No. HIT.KLOF.MST.2018028).

References

[1] B. B. Yan, R. F. Liu, P. Dai, M. Z. Xing, and S. X. Liu, "A rapid penetration trajectory optimization method for hypersonic vehicles," *International Journal of Aerospace Engineering*, vol. 2019, 11 pages, 2019.

[2] M. J. Wu, Z. W. Shi, T. H. Xiao, and H. S. Ang, "Flight trajectory optimization of sun-tracking solar aircraft under the constraint of mission region," *Chinese Journal of Aeronautics*, vol. 34, no. 11, pp. 140–153, 2021.

[3] S. W. Hur, S. H. Lee, Y. H. Nam, and C. J. Kim, "Direct dynamic-simulation approach to trajectory optimization," *Chinese Journal of Aeronautics*, vol. 34, no. 10, pp. 6–19, 2021.

[4] B. Jiang, D. Qi, C. L. Yang et al., "Modern optimization theory and applications," *Scientia Sinica(Mathematica)*, vol. 50, no. 7, pp. 899–968, 2020.

[5] R. Q. Chai, A. Tsourdos, A. Savvaris, S. C. Chai, Y. Q. Xia, and C. L. P. Chen, "Review of advanced guidance and control algorithms for space/aerospace vehicles," *Progress in Aerospace Sciences*, vol. 122, p. 100696, 2021.

[6] R. Q. Chai, A. Tsourdos, A. Savvaris, S. C. Chai, and Y. Q. Xia, "A review of optimization techniques in spacecraft flight trajectory design," *Progress in Aerospace Sciences*, vol. 109, p. 100543, 2019.

[7] S. Zhai and J. Y. Yang, "Piecewise analytic optimized ascent trajectory design and robust adaptive finite-time tracking control for hypersonic boost-glide vehicle," *Journal of the Franklin Institute*, vol. 357, no. 9, pp. 5485–5501, 2020.

[8] G. N. Kumar, D. Penchalaiah, A. K. Sarkar, and S. E. Talole, "Hypersonic boost glide vehicle trajectory optimization using

genetic algorithm-sciencedirect," *IFAC-PapersOnLine*, vol. 51, no. 1, pp. 118–123, 2018.

[9] J. Lin, Y. Z. He, and P. X. Huang, "Powered hypersonic vehicle reentry trajectory optimization based on improved multi-phase gauss spectral method," *Control Theory and Applications*, vol. 36, no. 10, pp. 1662–1671, 2019.

[10] H. H. Kwon, S. M. Hong, G. H. Kim, and Y. H. Kim, "Mid-course trajectory optimization for boost-glide missiles based on convex programming," *Journal of the Korean Society for Aeronautical & Space Sciences*, vol. 49, no. 1, pp. 21–30, 2021.

[11] X. D. Yan, S. Lyu, and S. Tang, "Analysis of optimal initial glide conditions for hypersonic glide vehicles," *Chinese Journal of Aeronautics*, vol. 27, no. 2, pp. 217–225, 2014.

[12] P. Lu and S. Xue, "Rapid generation of accurate entry landing footprints," *Journal of Guidance Control & Dynamics*, vol. 33, no. 3, pp. 756–767, 2010.

[13] R. Q. Chai, A. Tsourdos, A. Savvaris, S. C. Chai, Y. Q. Xia, and C. L. P. Chen, "Six-DOF spacecraft optimal trajectory planning and real-time attitude control: a deep neural network-based approach," *IEEE Transactions on Neural Networks and Learning Systems*, vol. 31, no. 11, pp. 5005–5013, 2019.

[14] R. Q. Chai, A. Tsourdos, A. Savvaris, Y. Q. Xia, and S. C. Chai, "Real-time reentry trajectory planning of hypersonic vehicles: a two-step strategy incorporating fuzzy multiobjective transcription and deep neural network," *IEEE Transactions on Industrial Electronics*, vol. 67, no. 8, pp. 6904–6915, 2020.

[15] R. Q. Chai, A. Savvaris, A. Tsourdos, S. C. Chai, and Y. Q. Xia, "Stochastic spacecraft trajectory optimization with the consideration of chance constraints," *IEEE Transactions on Control Systems Technology*, vol. 28, no. 4, pp. 1550–1559, 2020.

[16] R. Q. Chai, A. Savvaris, A. Tsourdos, S. C. Chai, and Y. Q. Xia, "Trajectory optimization of space maneuver vehicle using a hybrid optimal control solver," *IEEE Transactions on Cybernetics*, vol. 49, no. 2, pp. 467–480, 2019.

[17] R. Q. Chai, A. Savvaris, A. Tsourdos, S. C. Chai, and Y. Q. Xia, "Unified multiobjective optimization scheme for aeroassisted vehicle trajectory planning," *Journal of Guidance Control & Dynamics*, vol. 41, no. 7, pp. 1521–1530, 2018.

[18] Q. Shi and H. Zhang, "Road-curvature-range-dependent path following controller design for autonomous ground vehicles subject to stochastic delays," *IEEE Transactions on Intelligent Transportation Systems*, pp. 1–11, 2022.

[19] M. Bittner, F. Fisch, and F. Holzapfel, "A multi-model gauss pseudospectral optimization method for aircraft trajectories," in *AIAA Atmospheric Flight Mechanics Conference*, Minneapolis, America, 2012.

[20] G. T. Huntington, *Advancement and analysis of gauss pseudospectral transcription for optimal control problems*, Massachusetts Institute of Technology, 2007.

[21] M. Lin, Z. J. Shao, W. F. Chen, X. G. Lv, and Z. Y. Song, "Three-dimensional trajectory optimization for lunar ascent using Gauss pseudospectral method," in *AIAA Guidance, Navigation, & Control Conference*, San Diego, California, USA, 2016.

[22] C. Y. Liu and C. Zhang, "Multi-stage trajectory optimization of tactical two-stage booster rocket based on gauss pseudospectral method," *Acta Armamentarii*, vol. 40, no. 2, pp. 292–302, 2019.

[23] R. Q. Chai, A. Savvaris, and A. Tsourdos, "Fuzzy physical programming for space manoeuvre vehicles trajectory optimization based on hp-adaptive pseudospectral method," *Acta Astronautica*, vol. 123, pp. 62–70, 2016.

[24] K. J. Chen, L. H. Liu, and Y. H. Meng, *Launch vehicle flight dynamics and guidance*, National Defense Industry Press, Beijing, 2014.

[25] Y. Lecun, Y. Bengio, and G. Hinton, "Deep learning," *Nature*, vol. 521, no. 7553, pp. 436–444, 2015.

[26] M. A. Nielsen, *Neural Networks and Deep Learning*, Determination Press, San Francisco, America, 2015.

[27] J. Bergstra and Y. Bengio, "Random search for hyper-parameter optimization," *The Journal of Machine Learning Research*, vol. 13, pp. 281–305, 2012.

[28] G. Montavon, G. B. Orr, and K. R. Müller, *Neural Networks: Tricks of the Trade*, Springer, Berlin, Heidelberg, 2012.

[29] A. Alessandretti, A. P. Aguiar, and C. N. Jones, "Trajectory-tracking and path-following controllers for constrained under-actuated vehicles using model predictive control," in *2013 European Control Conference*, pp. 1371–1376, Zurich, Switzerland, July 2013.

[30] X. S. Chen, H. Mai, Z. M. Zhang, and F. Q. Gu, "A novel adaptive pseudospectral method for the optimal control problem of automatic car parking," *Asian Journal of Control*, vol. 24, no. 3, pp. 1363–1377, 2022.

[31] X. Q. Jiang, S. Li, and R. Furfaro, "Integrated guidance for Mars entry and powered descent using reinforcement learning and pseudospectral method," *Acta Astronautica*, vol. 163, pp. 114–129, 2019.

[32] R. Q. Chai, A. Savvaris, and A. Tsourdos, "Violation learning differential evolution-based hp-adaptive pseudospectral method for trajectory optimization of space maneuver vehicle," *IEEE Transactions on Aerospace and Electronic Systems*, vol. 53, no. 4, pp. 2031–2044, 2017.

[33] H. Y. Hou, W. Hager, and A. Rao, "Convergence of a Gauss pseudospectral method for optimal control," in *AIAA Guidance, Navigation, & Control Conference*, Minneapolis, America, 2012.

[34] Z. B. Zhao, B. Liu, C. R. Zhang, and H. R. Liu, "An improved adaptive NSGA-II with multi-population algorithm," *Applied Intelligence*, vol. 49, no. 2, pp. 569–580, 2019.